

Formation of the Hub-Filament System G33.92+0.11: Local Interplay between Gravity, Velocity, and Magnetic Field

JIA-WEI WANG,^{1,2} PATRICK M. KOCH,¹ ROBERTO GALVÁN-MADRID,³ SHIH-PING LAI,² HAUYU BAOBAB LIU,¹
SHENG-JUN LIN,² AND KATE PATTLE^{4,2}

¹*Academia Sinica Institute of Astronomy and Astrophysics, No.1, Sec. 4., Roosevelt Road, Taipei 10617, Taiwan*

²*Institute of Astronomy and Department of Physics, National Tsing Hua University, Hsinchu 30013, Taiwan*

³*Instituto de Radioastronomía y Astrofísica, Universidad Nacional Autónoma de México, Apdo. Postal 3-72 (Xangari), 58089 Morelia, Michoacán, Mexico*

⁴*Centre for Astronomy, School of Physics, National University of Ireland Galway, University Road, Galway, Ireland*

(Accepted 2020/11/3)

Submitted to ApJ

ABSTRACT

The formation of filaments in molecular clouds is an important process in star formation. Hub-filament systems (HFSs) are a transition stage connecting parsec-scale filaments and proto-clusters. Understanding the origin of HFSs is crucial to reveal how star formation proceeds from clouds to cores. Here, we report JCMT POL-2 850 μm polarization and IRAM 30-m C¹⁸O (2-1) line observations toward the massive HFS G33.92+0.11. The 850 μm continuum map reveals four major filaments converging to the center of G33.92+0.11 with numerous short filaments connecting to the major filaments at local intensity peaks. We estimate the local orientations of filaments, magnetic field, gravity, and velocity gradients from observations, and we examine their correlations based on their local properties. In the high-density areas, our analysis shows that the filaments tend to align with the magnetic field and local gravity. In the low-density areas, we find that the local velocity gradients tend to be perpendicular to both the magnetic field and local gravity, although the filaments still tend to align with local gravity. A global virial analysis suggests that the gravitational energy overall dominates the magnetic and kinematic energy. Combining local and global aspects, we conclude that the formation of G33.92+0.11 is predominantly driven by gravity, dragging and aligning the major filaments and magnetic field on the way to the inner dense center. Traced by local velocity gradients in the outer diffuse areas, ambient gas might be accreted onto the major filaments directly or via the short filaments.

Keywords: ISM: clouds — ISM: magnetic fields — ISM: structure — ISM: individual objects (G33.92+0.11) — ISM: kinematics and dynamics

1. INTRODUCTION

Herschel observations of the Galactic interstellar medium revealed that filamentary structures are ubiquitous in molecular clouds, and that they are a key intermediate stage towards the formation of stars (e.g., André et al. 2010; Arzoumanian et al. 2011; André et al. 2014). Embedded in these filaments, many stars appear to form within clustered environments (e.g., Lada & Lada 2003; Gutermuth et al. 2009; Kirk et al. 2013). Myers (2009) reviewed previous observations and suggested that protoclusters are commonly associated with

hub-filament systems (HFSs), where they are formed in a dense hub with numerous radial filaments extending from the central hub. Understanding how HFSs form is a topic of considerable interest, since HFSs are the possible transition stage connecting the evolution of filamentary clouds and the formation of protoclusters (e.g., Schneider et al. 2012).

The origin of HFSs is still under debate. Observationally, HFS are seen across a variety of physical scales and environments, from the IRDC G335.43–0.24 with a physical size of ~ 5 pc (Myers 2009) to the ~ 0.3 -pc-sized HFS embedded within the Orion integral filament (Hacar et al. 2018). As these HFSs are identified only based on their morphologies, the question re-

mains whether all these systems form via similar mechanisms. Theoretical works suggest that HFS-like morphologies can be formed by a diversity of different mechanisms, such as layer fragmentation threaded by magnetic fields (Myers 2009; Van Loo et al. 2014), magnetic field channeled gravitational collapse (e.g., Nakamura & Li 2008), shock/turbulence compression (e.g., Padoan et al. 2001b; Federrath 2016), multi-scale gravitational collapse (e.g., Gómez & Vázquez-Semadeni 2014; Gómez et al. 2018), and filament collisions (e.g., Nakamura et al. 2014; Dobashi et al. 2014; Frau et al. 2015). To further constrain these theories, it is crucial to observe key physical parameters related to these proposed physical mechanisms, such as velocity structures and magnetic fields.

Recent molecular line observations have revealed the kinematic structures of HFSs in nearby clouds. The line of sight (LOS) velocity gradient, traced by molecular lines, is commonly interpreted as a proxy for the plane-of-sky (POS) gas motion. Significant velocity gradients along filaments are seen in several HFSs (e.g., Friesen et al. 2013; Liu et al. 2012a; Hacar et al. 2018; Chen et al. 2020b), suggesting that these filaments are likely dynamical gas flows and not static structures. The comparison between the density structures and the direction of the velocity gradient further suggests that these gas flows are possibly driven by gravity (e.g., Friesen et al. 2013; Hacar et al. 2018). Local velocity gradients within HFSs have been measured in a few systems (e.g., Peretto et al. 2014; Williams et al. 2018; Chen et al. 2020b). These observations reveal a variation of velocity structures possibly influenced by shock compression (Williams et al. 2018) or the balance between gas pressure and gravity (Chen et al. 2020b). Nevertheless, as molecular line observations only trace the LOS velocity, its gradient might also have a different origin, such as cloud collision, rather than the POS gas flows (Li & Klein 2019). Hence, the alone analysis of LOS velocity gradients needs caution, and a joint analysis with additional measured physical parameters can lead to further insight (Tang et al. 2019).

Magnetic fields can be a key factor in the formation of molecular clouds and filaments, but their exact role is still uncertain (Li et al. 2014). Strong magnetic fields might constrain the gravitational collapse/fragmentation (e.g., Nakamura & Li 2008; Myers 2009; Van Loo et al. 2014), channel turbulent flows (e.g., Stone et al. 1998; Li & Houde 2008), and guide accreting gas (e.g., André et al. 2014; Shimajiri et al. 2019). At pc-scale, starlight polarization observations often reveal organized magnetic fields perpendicular to the longer axis of HFSs (e.g., Sugitani et al. 2011; Santos et al.

2016; Wang et al. 2020), which has been interpreted as evidence for strong magnetic field models. However, other simulations suggest that the observed configurations can also be reproduced by mechanisms, such as multi-scale gravitational collapse (e.g., Gómez et al. 2018) and shock compression (e.g., Chen et al. 2020a). The recent JCMT BISTRO survey (Ward-Thompson et al. 2017) is probing the 1–0.01 pc scales magnetic fields toward numerous star-forming regions, including several known HFSs, such as IC5146 (Wang et al. 2019), NGC1333 (Doi et al. 2020), NGC6334 (Arzoumanian et al. 2020). The BISTRO survey has revealed locally organized magnetic fields, displaying a variety of magnetic field morphologies around HFSs along filaments, possibly caused by a variable energy balance between gravity and magnetic field. These results suggest that the role of the magnetic field in HFSs is possibly scale-dependent and varies with the environments (e.g., Wang et al. 2019; Arzoumanian et al. 2020). However, polarization observations toward HFSs are still rare, and thus, more observational samples are still required to conclude on the role of magnetic fields in the formation of HFSs.

G33.92+0.11 is a remarkable ultracompact HII region that lies $7.1_{-0.3}^{+1.2}$ kpc away in the Galactic plane (Fish et al. 2003). Since its derived virial mass (G33.92+0.11 A: $520 M_{\odot}$; G33.92+0.11 B: $270 M_{\odot}$) is much smaller than its enclosed molecular gas mass (G33.92+0.11 A: $5100 M_{\odot}$; G33.92+0.11 B: $3200 M_{\odot}$), it is likely geometrically thin and face-on (Watt & Mundy 1999; Liu et al. 2012a). Thus, it is a good example to reveal the detailed morphology of an HFS. Liu et al. (2012a) observed the 1.3 mm continuum emission within the inner 2 pc area of G33.92+0.11 and found that the system is composed of pc-long filaments converging to a massive ($3.0_{-1.4}^{+2.8} \times 10^3 M_{\odot}$) hub within the inner 0.6 pc, making this a typical HFS morphology. Liu et al. (2015) performed ALMA observations toward this central 0.6 pc area using several molecular lines. They found that this center contains several spiral-like filaments converging to two central massive ($100\text{--}300 M_{\odot}$) molecular cores. The 1000-au resolution 225 GHz continuum ALMA observations further identified 28 Class 0/I YSO candidates around these two massive cores, indicating that the center of this HFS is associated with cluster formation (Liu et al. 2019). These results reveal a picture where a massive protocluster can form within a central hub fed by gravitationally driven flows from 1-pc to 1000-au scales.

In this paper, we report the polarization and molecular line observations toward the G33.92+0.11 system, using the JCMT POL-2 polarimeter and the IRAM 30-m telescope. These observations, with a resolution of ~ 0.5 pc, allow us to probe the magnetic field and kinematic

structures of the G33.92+0.11 HFS at pc-scale. We aim at investigating how gravitational and magnetic fields interact with the density and kinematic structures in order to understand the formation of the G33.92+0.11 HFS. In Section 2, we present the observations and data reduction. Section 3 reports the observed magnetic field map and the kinematic structures of this system. Section 4 presents how we estimate the filamentary density structures, the local velocity gradient, and the local gravitational force from the observed data. A statistical analysis is performed to identify possible correlations between these physical parameters. We discuss the dynamics of the system and its possible origin in Section 5. Our conclusions are summarized in Section 6.

2. OBSERVATIONS

2.1. JCMT POL-2 Observations

We carried out polarization continuum observations toward G33.92+0.11 with the reference position (R.A., Dec.)=(18^h52^m50.4^s, 00°55′28″9) with SCUBA2 POL-2 mounted on the JCMT (project code M19AP034; PI: Jia-Wei Wang). Our target was observed with 24 sets of 40-minute integration between 2019 May 13 and 2019 June 2 under a τ_{225GHz} opacity ranging from 0.03 to 0.06. The POL-2 DAISY scan mode (Friberg et al. 2016) was adopted, producing a fully sampled circular region with a diameter of 11′ and a resolution of 14″, leading to a map with lowest and nearly uniform noise within the central 3 arcmin diameter region, and increasing noise towards the edge of the map. Both the 450 and 850 μm continuum polarization were observed simultaneously. This paper focuses on the 850 μm data.

The POL-2 polarization data were reduced using *pol2map*¹ in the SMURF package² (Berry et al. 2005; Chapin et al. 2013). The reduction procedure followed the *pol2map* script. The *skyloop* mode was invoked in order to reduce the uncertainty generated during the map-making process, which grows with intensities. The MAPVARS mode was activated, with which the uncertainty of the co-added images was calculated from the standard deviation among the individual observations, to account for the uncertainty of the map-making process in the error estimation. The details of the data reduction steps and procedure are described in a series of BISTRO papers (e.g., Ward-Thompson et al. 2017; Kwon et al. 2018; Wang et al. 2019). The POL-2 data reduction was done with a 4″ pixel size, because larger pixel sizes can increase the uncertainty due to the

map-making process. It is worth noting that JCMT observations use a chopping mode and high-pass filtering to remove background atmospheric emission. This also filters out extended source structures with scales $\gtrsim 3'$. This filtering does not affect our analysis because the physical size of G33.92+0.11 is about 3′, but helps to remove possible contamination from extended background and foreground emission.

The output Stokes I, Q, and U images were calibrated in units of mJy/beam, using a flux conversion factor (FCF) of 725 mJy/pW (Dempsey et al. 2013), and binned to a pixel size of 12″ to improve the sensitivity. The polarization fraction and orientations were calculated for each 12″ pixel, which is close to the beam size of 14″, hence yielding nearly independent measurements. The typical rms noise of the final Stokes Q and U maps is ~ 1.1 mJy beam⁻¹ at the center of the map. The Stokes I image has a higher intensity-dependent rms noise, 1–5 mJy beam⁻¹ near the center of the map, as a result of the uncertainties due to the map-making process.

We debiased the polarization fraction with the asymptotic estimator (Wardle & Kronberg 1974) as

$$P = \frac{1}{I} \sqrt{(U^2 + Q^2) - \frac{1}{2}(\sigma_Q^2 + \sigma_U^2)}, \quad (1)$$

where P is the debiased polarization percentage, and I , Q , U , σ_I , σ_Q , and σ_U are the Stokes I , Q , U , and their uncertainties. The uncertainty of the polarization fraction was estimated using

$$\sigma_P = \sqrt{\frac{(Q^2\sigma_Q^2 + U^2\sigma_U^2)}{I^2(Q^2 + U^2)} + \frac{\sigma_I^2(Q^2 + U^2)}{I^4}}. \quad (2)$$

The polarization position angle (PA) was calculated as

$$PA = \frac{1}{2} \tan^{-1}\left(\frac{U}{Q}\right), \quad (3)$$

and its corresponding uncertainty was estimated using

$$\sigma_{PA} = \frac{1}{2} \sqrt{\frac{(Q^2\sigma_U^2 + U^2\sigma_Q^2)}{(Q^2 + U^2)^2}}. \quad (4)$$

2.2. IRAM 30-m Observations

The C¹⁸O (2-1) emission line can trace dense gas with a density of $\sim 10^4$ cm⁻³ (e.g., Nishimura et al. 2015), comparable to the typical densities of pc-scale filaments (e.g., André et al. 2014). Aiming at probing gas kinematics within filaments, C¹⁸O (2-1) spectral line observations were performed with the IRAM 30-m telescope on November 20, 2011 using the on-the-fly mapping mode (project 179-11, PI:Hauyu Baobab Liu) toward

¹ <http://starlink.eao.hawaii.edu/docs/sc22.pdf>

² version 2019 Nov 2

G33.92+0.11 (R.A.= $18^h52^m50.2^s$ and Dec.= $0^\circ55'30''0$). The scan produced a $6' \times 6'$ map, covering both the G33.92+0.11 hub and the surrounding filaments. The observations were carried out with the HERA receiver tuned at 219.755 GHz and the FTS spectrometer as the spectral backend with a spectral resolution of 50 kHz, 0.066 km s^{-1} , and a bandwidth of 625 MHz. At this frequency, the telescope delivered a beam size of $11.8''$. The data were reduced with the standard procedure with the CLASS package of the GILDAS³ software (Pety 2005; Gildas Team 2013). To improve the sensitivity, we binned the data to a spatial resolution of $14''$. The resulting typical rms noise of the smoothed data was 0.2 K.

3. RESULTS

3.1. Dust Continuum

Assuming that the observed polarization traces magnetically aligned dust grains (e.g., Cudlip et al. 1982; Hildebrand 1988), we rotate the polarization segments by 90° and show the resulting magnetic field orientations with a pixel size of $12''$, overlaid on the Stokes I map with a pixel size of $4''$ in Figure 1. The total intensity image clearly shows a bright central hub at the center of G33.92+0.11, surrounded by faint extended structures. In addition to the major central hub, a second minor hub (hereafter western hub) can be seen west of the central hub. This western hub is connected to the central hub through two bridging filaments. Contours are additionally used in Figure 1 to emphasize connecting structures. In particular the lower contours around the central hub are not simply circular, but they reveal extensions to the south and west, likely indicating the presence of filaments connecting to the central hub.

3.2. Polarization Data Selection

In order to ensure significant detections, we limit polarization segments to $I/\sigma_I > 10$ and $P/\sigma_P > 2$ within the field of Figure 1. The selected 152 polarization measurements include 91 segments with $P/\sigma_P > 3$ and 61 segments with $3 > P/\sigma_P > 2$. The $P/\sigma_P > 3$ sample has a maximum σ_{PA} of 9.3° with a mean σ_{PA} of 5.7° . The $3 > P/\sigma_P > 2$ sample has a maximum σ_{PA} of 13.0° with a mean σ_{PA} of 10.7° . The distribution of the polarization fraction and how the polarization fraction is related to the total intensity is reported in Appendix A, where we examine whether the observed polarization traces magnetically aligned dust grains.

3.3. Magnetic Field Morphology

The observed magnetic field morphology shows an overall converging feature: the field is prevalingly north-to-south (PA $\sim 0^\circ$) on the northern and the south-eastern side of the central hub, and it is east-west (PA $\sim 90^\circ$) in the west with some segments to the east that appear to be bent and turning to the center. Around the western hub, the field is along a northwest-southeast orientation (PA $\sim 120^\circ$) in the west, and it is more northeast-southwest (PA $\sim 40^\circ$) on the eastern side, becoming almost parallel to the bridging filaments connecting to the central hub. Additionally, the changes in field orientations are mostly smooth, as the local magnetic field often displays an orientation similar to adjacent segments. Since the polarization segments are plotted per independent beam ($14'' = 0.5 \text{ pc}$), adjacent segments are mostly uncorrelated, and thus the observed features indicate that the magnetic field morphology indeed varies smoothly over parsec-scale.

3.4. Gas Kinematics

In order to reveal the gas motion within G33.92+0.11, we performed Gaussian fits of the C^{18}O spectra pixel by pixel, using the python package PySpecKit (Ginsburg & Mirocha 2011), to estimate the gas centroid velocity and velocity dispersion. The pixels with a signal-to-noise ratio (SNR) < 3 in the data cube were excluded from the fit. As most of the spectra show only one dominant component, we used a single-Gaussian model to trace the major gas motion. The C^{18}O integrated intensity, centroid velocity, and the velocity dispersion maps are shown in Figure 2. We note that a few spectra in the hub center show possible multiple components. However, this is not a concern for our work here because we are focusing on the connecting extended structures towards the hub, and it is not our goal to resolve the more complicated velocity structure inside the central hub region.

The integrated intensity map (left panel in Figure 2) reveals a similar hub-filament morphology as seen in the dust continuum. Additionally, it resolves two fragmented cores within the central hub, which is visible but less obvious in the continuum image. Nevertheless, some of the faint extended continuum structures are not visible in the C^{18}O image due to its lower SNR. The C^{18}O centroid velocity map (middle panel in Figure 2) presents several band-like structures where the LOS velocities are roughly similar. For example, a band with a LOS velocity of $107\text{--}108 \text{ km s}^{-1}$ (yellow to red) extends from the hub center to the north-west and to the south-east. Another band with a LOS velocity of $\sim 106.5 \text{ km s}^{-1}$ (green) extends from the center to the south and to the north-east. The derived C^{18}O veloc-

³ available at <http://www.iram.fr/IRAMFR/GILDAS>

ity dispersion (right panel in Figure 2) clearly increases from outside to inside, and the locations of the peak velocity dispersions match the central hub and some local intensity peaks. This peaks in dispersion can possibly be caused by gravitational acceleration.

In summary, the similar features and extensions seen in the IRAM 30-m line and the JCMT 850 μm continuum data together with their very good spatially overlapping coverage suggest that the two data sets are tracing the same underlying structures. This forms our basis to further investigate how local gas motions correlate with the magnetic field.

4. ANALYSIS

In the following sections, we aim at extracting the spatial properties of the filamentary structures, the local gravitational force, and the local velocity gradient. Together with the observed magnetic field morphology, these properties are used to investigate how these physical quantities possibly correlate with each other *locally*. The local aspect is central here because we are aiming at studying the detailed interplay between the various parameters which is not possible from an analysis of global properties alone.

4.1. Filament Identification

In order to identify the ridges of filamentary structures in the JCMT 850 μm Stokes I image we adopt the *DisPerSE* algorithm (Sousbie 2011). This algorithm is designed to identify topological features within an image based on the Morse Theory. *DisPerSE* first identifies the critical points (maxima, minima, and saddle points) in an image. Filaments are then identified as a series of multiple maxima-saddle point pairs connected by segments tangent to the intensity gradient field. In order to filter out insignificant structures, an intensity contrast threshold, named persistence threshold, is applied to exclude those maxima-saddle point pairs where the intensity differences are less than the threshold. The resolution of the identified filaments is roughly equal to that of the input image ($4''$), which is adequate to sample our beam size ($14''$).

Figure 3(a) shows the identified filaments with thresholds of 20 and 25 mJy beam^{-1} , respectively. These thresholds correspond to a level of 4 and 5σ , where σ is the maximum rms noise of 5 mJy beam^{-1} near the image center. The filamentary networks identified with the two thresholds both present converging features. The longer filaments all connect to the major converging points (C1 and C2). The shorter filaments either connect to C1 and C2, or merge into the longer filaments at the minor converging points (C3–C6). The major converging points

coincide with the positions of the central and western hub, and the minor converging points match the local intensity peaks.

Figure 3(b) further displays the identified filaments overlaid on the C^{18}O integrated intensity map. As the C^{18}O integrated intensity map reveals a morphology similar to the 850 μm continuum map, the identified filaments also roughly trace the filamentary structure in the C^{18}O intensity map. The converging points C1 and C3 match the locations of the two C^{18}O intensity peaks, revealing two fragmented cores, within the central hub. Nevertheless, since the SNR in the C^{18}O integrated intensity map is much lower than in the 850 μm continuum map, some of the fainter filaments are less apparent. As a consequence, our further analysis is based on the filaments identified from the 850 μm continuum map. Moreover, we will mainly use the filaments identified with the higher persistence threshold of 25 mJy beam^{-1} in order to identify high-SNR features. The possible bias due to the selected threshold is discussed in Appendix B.

In order to estimate the filament width, we use the python package *FilChap*⁴ (Suri et al. 2019). Since the intensity of the identified filaments often varies significantly, e.g., from tens of mJy beam^{-1} in the faint envelope to thousands of mJy beam^{-1} in the central hub, we do not expect the filament widths to be constant along the filaments. Hence, we fit individual radial intensity profiles extracted at each pixel position along the filament ridge. We apply a bootstrap method to fit these radial profiles with a Gaussian function. To estimate the fitting uncertainties, we use a Monte Carlo approach to generate 100 simulated profiles based on the observed intensities and uncertainties. The uncertainties of the fitting parameters are then estimated from the standard deviation of the fitting results to the 100 simulated samples. Fits with a width smaller than three times the uncertainties are excluded from the further analysis. The fitted Gaussian widths (σ_F) are deconvolved and converted to the FWHM (ΔF_{deconv}) via $\Delta F_{deconv}^2 = 8 \ln 2 \sigma_F^2 - \theta_{beam}^2$, where θ_{beam} is the JCMT beam size (0.48 pc). An example of the radial intensity profile with its best fit is shown in Figure 4.

Figure 5(a) shows the histogram of all deconvolved filament widths, mostly ranging from 0.4 to 0.6 pc. This is comparable to our spatial resolution of 0.48 pc. Thus, our data can only marginally resolve the filaments, and consequently are insufficient to probe the internal structure within the filaments. Figure 5(b) illustrates

⁴ Bugs in the Dec 2018 version of *FilChap* were corrected prior to its application to the work here.

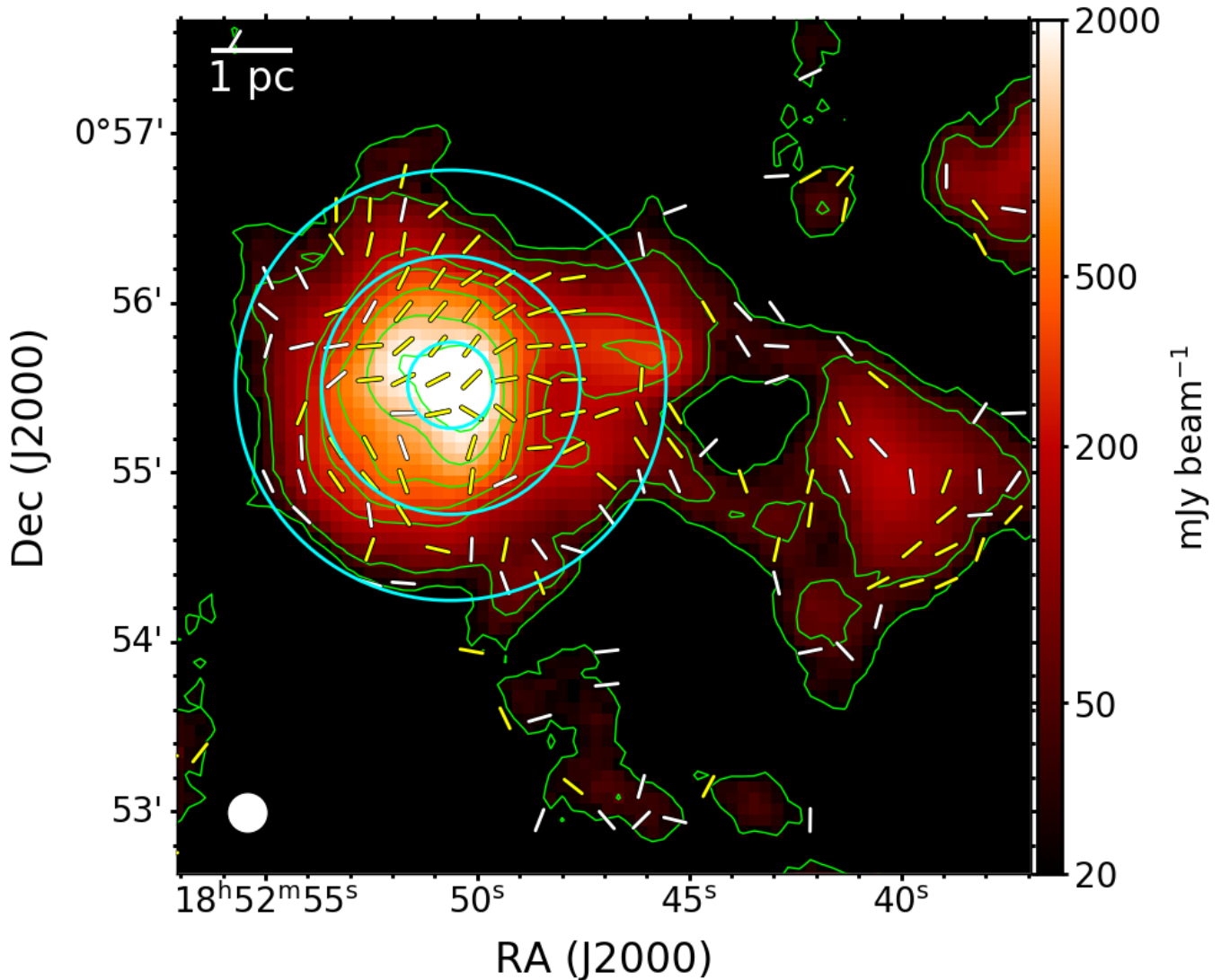


Figure 1. B-field orientations (segments) sampled on a $12''$ grid overlaid on $850 \mu\text{m}$ dust continuum (color and contours), sampled on a $4''$ grid, of the G33.92+0.11 region. The segments are selected with the criteria $I/\sigma_I > 10$ and $P/\sigma_P > 2$, and rotated by 90° to represent magnetic field orientations. The yellow and white segments display the larger than 3σ and $2\text{--}3\sigma$ polarization detections. The green contours show the total intensity at 20, 50, 200, 300, 500, 1000, and $2000 \text{ mJy beam}^{-1}$. The white circle in the bottom left corner is the JCMT beam size of $14''$. The white scale bar in the upper left corner denotes 1 pc. The cyan circles label the 1, 3, and 5 FWHM ($30.5''$) areas, where we perform the magnetic field strength estimate in Section 4.5. The Stokes I rms noise is $\sim 1\text{--}5 \text{ mJy beam}^{-1}$, depending on pixel intensities, within the central $3'$ area.

how the filament widths vary with the ridge intensities. The mean filament widths grow from 0.5 to 0.7 pc as the ridge intensities increase from <200 to $\sim 500\text{--}1000 \text{ mJy beam}^{-1}$, and they decrease again to ~ 0.5 pc as the ridge intensities grow beyond $2000 \text{ mJy beam}^{-1}$.

4.2. Local Gravitational Field

In order to investigate whether gravity influences the formation of the converging filaments, we estimate the projected gravitational vector field from the JCMT $850 \mu\text{m}$ continuum data. Since G33.92+0.11 is a distant object, foreground dust might bias the measured column

density. We have tried to estimate the temperature and column density from the *Herschel* 250, 350, and $500 \mu\text{m}$ continuum data, but found that the measured column density is generally too high ($\sim 10^{22} \text{ cm}^{-2}$) in the diffuse ($I_{850} < 100 \text{ mJy beam}^{-1}$) areas. In contrast, with the large-scale extended emission being filtered out by the JCMT scan mode, foreground contamination in the JCMT data is also minimized. The column density in the diffuse areas estimated from the JCMT $850 \mu\text{m}$ continuum data, adopting a constant temperature of 20 K from *Herschel* data, is consistent with the typical value of $\sim 10^{20}\text{--}10^{21} \text{ cm}^{-2}$. Hence, we are using the JCMT

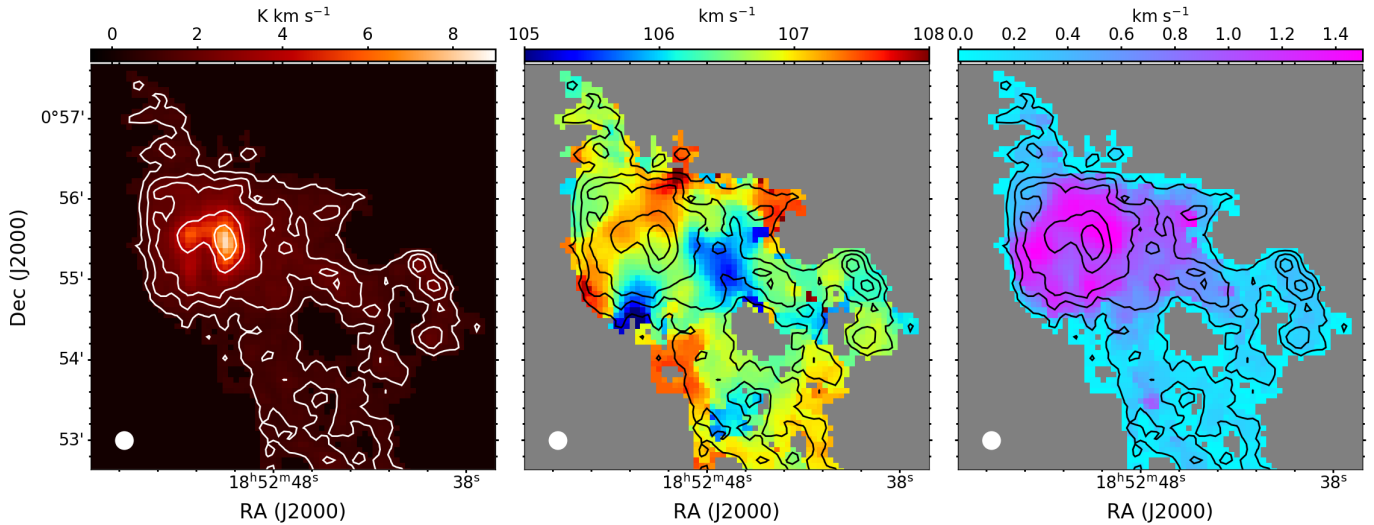


Figure 2. (a) IRAM 30-m C^{18}O (2-1) integrated intensity map, smoothed to a resolution of $14''$. The white contours represent integrated intensities of 1, 1.5, 2, 4, and 5 K km s^{-1} with an rms noise level of ~ 0.2 K. Clearly seen are two fragmented cores within the central hub, overlapping with the extended peak intensity region in the dust continuum map. (b) C^{18}O (2-1) centroid velocity map with integrated intensity contours. The velocity map reveals band-like patterns, along which the gas velocity only varies slightly. (c) C^{18}O (2-1) velocity dispersion (σ_v) map. The highest velocity dispersion regions coincide with the intensity peak, which is possibly related to the ongoing fragmentation as discussed in Section 5.3

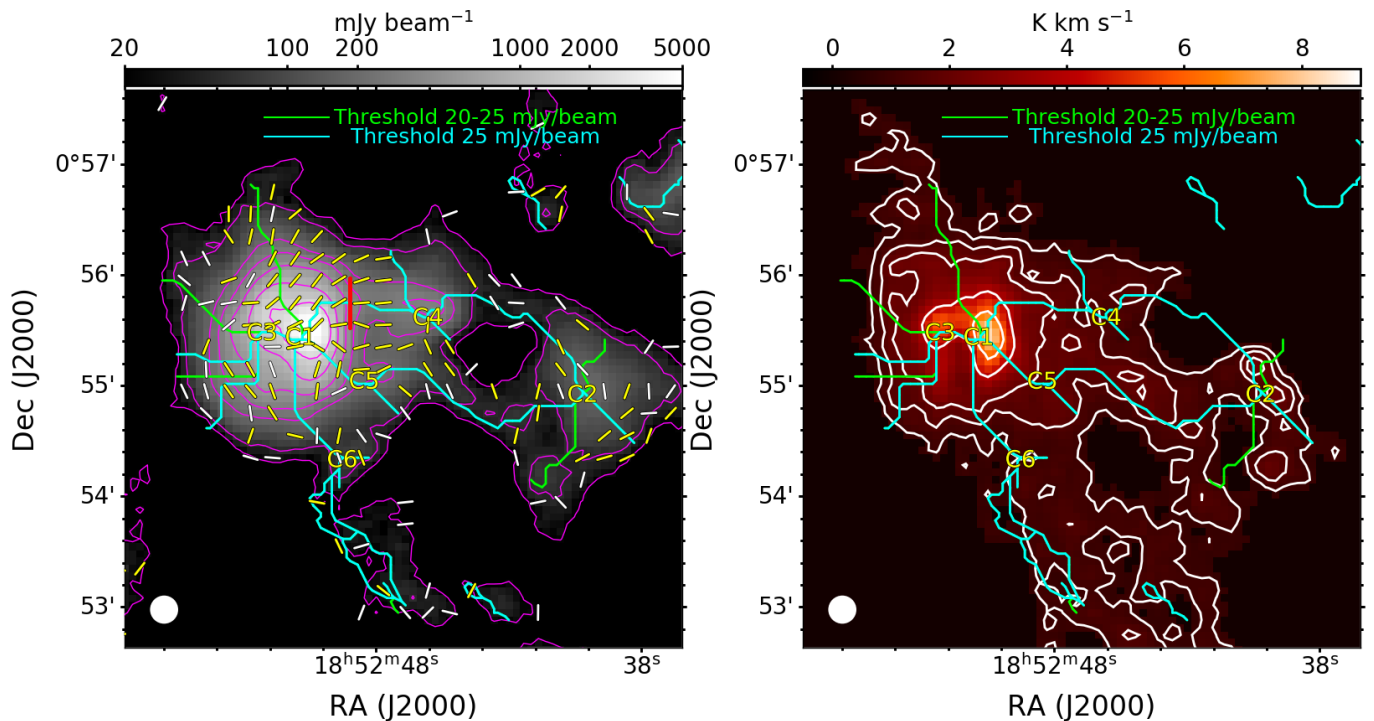


Figure 3. (a) Filaments identified in the $850 \mu\text{m}$ dust continuum map using the *DisPerSE* algorithm. The cyan filaments are identified with a threshold of >25 mJy/beam . Lowering the threshold to 20–25 mJy/beam leads to the additional filaments in green. The magenta contours show the $850 \mu\text{m}$ intensities of 20, 50, 200, 300, 500, 1000, and 2000 mJy/beam . C1 and C2 label the major filament converging points in the central and western hub. C3–C6 are minor converging points. The red segment illustrates a 9-pixel (~ 1.1 pc) cut perpendicular to the filament with a radial intensity profile shown in Figure 4. (b) Filaments identified as in panel (a), overlaid on the C^{18}O (2-1) integrated intensity map. The white contours denote integrated intensities of 1, 1.5, 2, 4, and 5 K km s^{-1} .

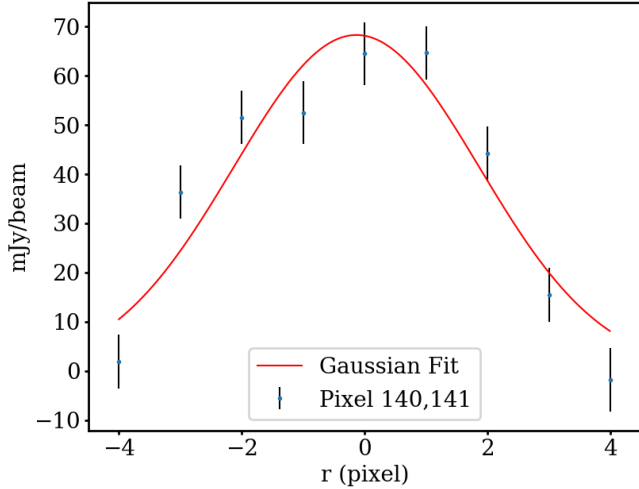


Figure 4. Example of filament radial intensity profile along the red cut shown in Figure 3. The red line shows its best-fit Gaussian. Measurement uncertainties are displayed with vertical error bars.

850 μm continuum data to derive the column density of our target.

Following the development of the polarization-intensity gradient technique in Koch et al. (2012a,b), the local projected gravitational force acting at a pixel position ($F_{G,i}$) can be expressed as the vector sum of all gravitational pulls generated from all surrounding pixel positions as

$$F_{G,i}^{\vec{r}} = k I_i \sum_{j=1}^n \frac{I_j}{r_{i,j}^2} \hat{r}, \quad (5)$$

where k is a factor accounting for the gravitational constant and conversion from emission to total column density. I_i and I_j are the intensity at the pixel position i and j , n is the total number of pixels within the area of relevant gravitational influence. $r_{i,j}$ is the plane-of-sky projected distance between the pixel i and j , and \hat{r} is the corresponding unity vector. The above equation assumes a constant conversion between dust and total column density. This leads to a *local gravitational vector field*, specifying a *local direction* and a *local magnitude* of the gravitational pull at every selected pixel. For our analysis here, we only focus on the directions of the local gravitational forces. Since we are not using the absolute magnitude, knowing the spatial distribution of dust is sufficient, assuming that its distribution is a fair approximation for the distribution of the total mass. In the above equation we thus assume $k=1$. When calculating the local gravitational field, a lower threshold for the surrounding diffuse and large-scale emission is introduced below which a gravitational influence is neglected. This is justified because this emission is weak and ad-

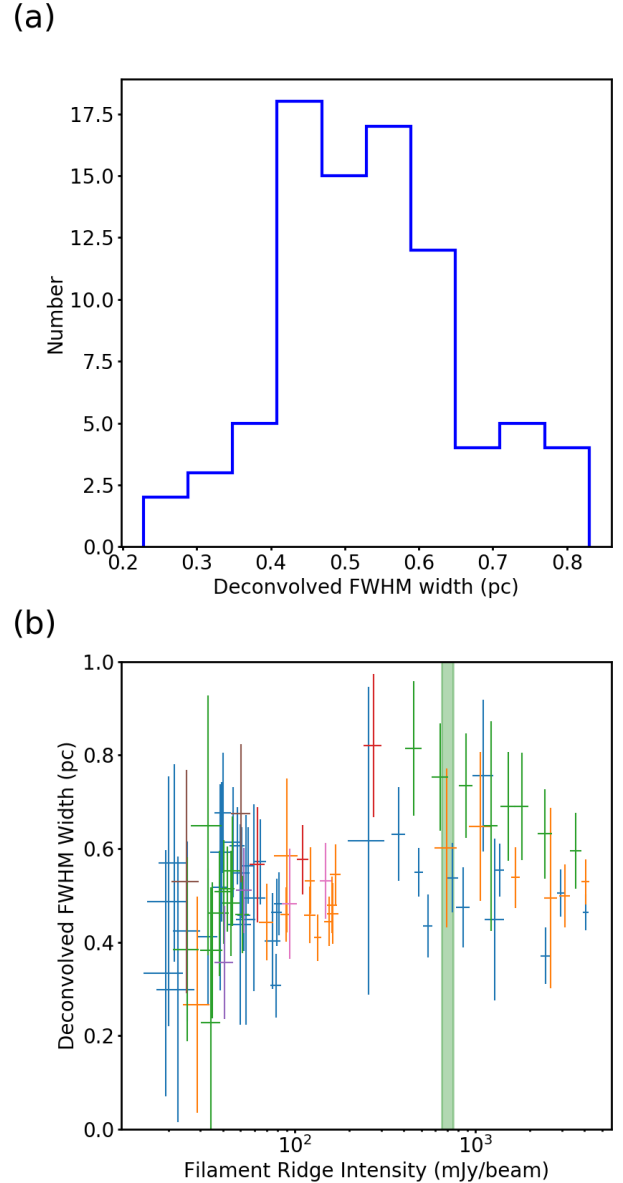


Figure 5. (a) Histogram of deconvolved filament widths. The widths are estimated from the radial intensity profiles at each pixel along the identified filament ridges, as illustrated in Figure 4. (b) Deconvolved filament widths vs. ridge intensities. Widths extracted along the same filament are shown with identical color. The filament width is not a constant. The mean width increases from 0.5 to 0.7 pc as the peak intensities increase from 200 to 1000 mJy beam^{-1} , and decreases again as the intensities increase beyond 1000 mJy beam^{-1} . The green area labels the critical linear density accounting for the support of thermal, non-thermal, and magnetic field pressure (see Section 5.1).

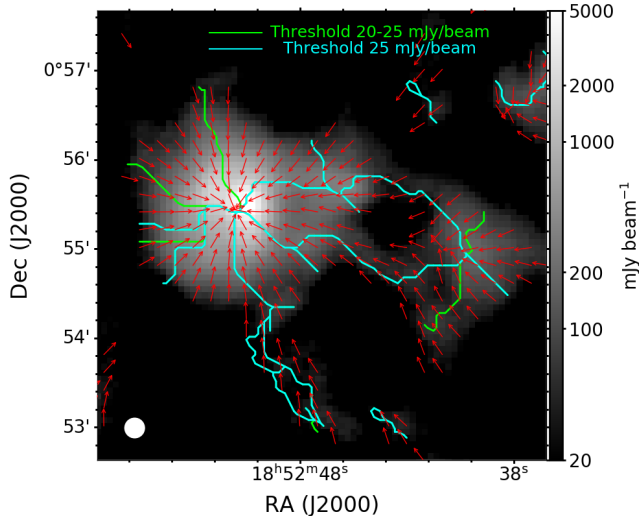


Figure 6. Projected local gravitational field (red arrows). The gravitational force vectors are displayed with uniform lengths to emphasize their directions. The green and cyan lines label the identified filaments as introduced in Figure 3(a). The projected gravitational field is converging to the central hub, similar to the identified filaments.

ditionally less important because of an increasing $1/r^2$ suppression in the above equation, and furthermore, this diffuse emission tends to be rather symmetrical which means that any small gravitational pulls largely cancel out. Based on this framework, the local role of gravity and magnetic field, their relative importance, spatial variations and systematic features, and statistical properties are interpreted and analyzed across a sample of 50 star-forming regions in Koch et al. (2013, 2014).

For our analysis we mask the pixels with an $850 \mu\text{m}$ intensity lower than 20 mJy beam^{-1} . Figure 6 displays the local gravitational vector field. In most of the areas, the local gravity is pointing toward the central hub. Around the western hub, the gravitational field is pointing toward the western hub on the western side, but on the eastern side, it is turning around to point to the more massive central hub. This morphology indicates that the massive central hub dominates the overall gravitational field in this area.

4.3. Local Velocity Gradient

In order to investigate whether the gas kinematics possibly correlate with the filamentary structures, we calculate velocity gradients from the C^{18}O centroid LOS velocity map (Figure 2(b)). In order to probe the local gas motion, we calculate *local* velocity gradients pixel by pixel, instead of only obtaining a global velocity gradient over an entire filament. To avoid calculating gradients from correlated pixels, the local velocity gradient at a pixel along the ridge of a filament is derived from

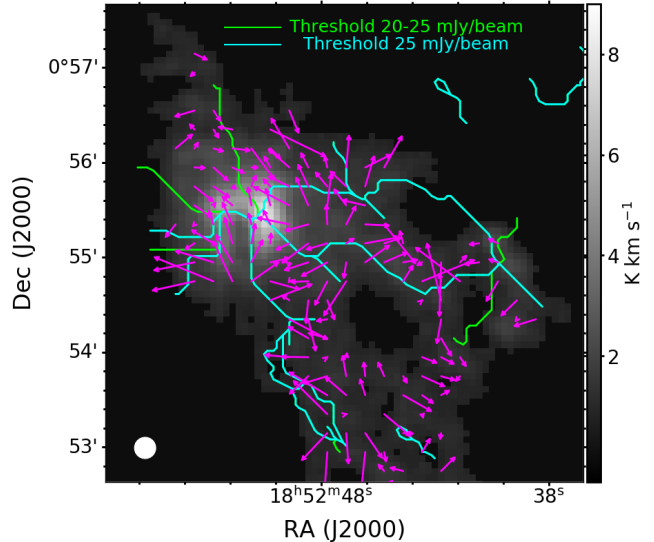


Figure 7. Local LOS velocity gradient field (magenta arrows) overlaid on the C^{18}O (2-1) integrated intensity map. The magnitude is proportional to the length of the arrows. The green and cyan lines are the identified filaments as introduced in Figure 3(a). In several locations, the directions of the local velocity gradients seem to be perpendicular to the filaments in the outer areas, but become more disordered nearing the central hub. The magnitude of the velocity gradient appears to decrease as the distance to the central hub decreases.

the centroid velocities of the four nearest neighbouring independent beams (separated by 3 pixels, $12''$). The resulting local velocity gradient field is plotted in Figure 7.

This velocity gradient field is less organized than the orientations of the filaments and the gravitational force field. It seems to be perpendicular to the filaments in the diffuser areas, but then changing to become more random near the central hub. The magnitude of the local velocity gradient appears to decrease as the distance to the central hub decreases. However, a more thorough statistical analysis is necessary to understand whether these trends are significant or not (see later in Section 5.3).

4.4. Correlations and Trends among Filaments, Magnetic Field, Gravity, and Gas Kinematics

4.4.1. Overall Statistical Correlations

To investigate how the physical parameters interact in the HFS, we perform systematic statistical analyses to reveal possible correlations among the orientations/directions of: filaments (F), magnetic fields (B), gravitational force (G), and gas velocity gradient (VG).

In order to estimate the filament orientations pixel by pixel, we select the identified filaments within 5 pc of

the central hub. The filaments made up of fewer than 6 pixels (≈ 2 independent beams) are excluded because they are not well resolved. For the i th pixel along the ridge of a filament, we fit the positions of the $(i-2)$ th to the $(i+2)$ th consecutive pixels along the filament with a straight line to estimate the local filament orientation.

We select the filament orientations, the magnetic field orientations, the gravitational force vectors, and the velocity gradients within 5 pc of the central hub as our sample to investigate their possible correlations. Figure 8 presents the histograms of the local orientations of filaments, magnetic field, gravity, and velocity gradients. Given the limited number of filaments, the resulting histogram shows two main peaks corresponding to the longest filaments extending to the west and southwest. The other three histograms display broad distributions with possibly again two broad though less pronounced peaks.

An all-pairwise comparison of the four parameters (F, B, G, VG) is performed. Parameters are spatially matched as following. For each measurement of one parameter, we select a nearest measurement of another parameter within a radius of $18''$ (1.5 beam). These two measurements are then defined as one associated pair for the two parameters. A differential orientation (ΔPA) is calculated for each associated pair. The resulting six distributions of all pairwise ΔPA are presented in Figure 9.

A Kolmogorov–Smirnov (KS) test is used to examine whether the ΔPA distributions differ from random distributions. For the KS test, we use a random distribution as the null hypothesis, and estimate the probability (p-value) of the random distribution to match the observed distribution. A threshold of $p=0.05$ (95% confidence interval) is used to reject the null hypothesis and identify the presence of a significant non-random trend. A significant non-random trend is further classified as parallel-like or perpendicular-like by whether the observed cumulative distribution is above or below the random distribution (diagonal line). The cumulative distributions of all six pairwise ΔPA are plotted in Figure 10. Among these pairs, the most significant correlation ($p < 0.001$) is found between local gravity and filament orientations (G vs F). This is expected because both the filaments and local gravity appear to overall converge towards the central hub, and consequently, the ΔPA distribution is clearly peaking at small values, and hence parallel-like. In addition, the orientations between local velocity gradient and magnetic field (VG vs B) are significantly non-random with $p = 0.004$. This ΔPA distribution reveals a trend of being perpendicular-like,

i.e., the local velocity gradient being perpendicular to the local magnetic field.

We note that a p-value higher than 0.05 only indicates that the observed ΔPA distribution is compatible with a random distribution. This can be caused by either an underlying randomly distributed ΔPA or a small sample size. Since our sample sizes in the denser area are often small, high p-values found for this area should not yet be taken as a final answer to not identifying any systematic structure in the data (see later section Section 4.4.3). Moreover, a KS test is not able to capture any possible spatial trends, as discussed in the following section.

4.4.2. Spatial Trends along Filaments

Histograms cannot visualize possible spatial trends among parameters. Therefore, we also show the ΔPA maps for the B-F, G-F, and VG-F pairs in Figure 11. Maps for all pairs are in Appendix B. These maps reveal that these ΔPA may vary along the filaments, possibly because the roles of these physical parameters change. Despite the overall statistical randomness between magnetic field and filament orientations (Figure 10), the B-F ΔPA map shows that the magnetic field appears to be more parallel to the filaments near the center of the dominating central hub, but occasionally becomes perpendicular to the short filaments connecting to the minor converging points C2, C3, and C4. This suggests that these short filaments might interact with the longer filaments differently. The G-F ΔPA map displays an alignment between gravity and filaments almost everywhere. There is non-alignment (local gravity perpendicular to filament) only in a few short filaments near the minor converging point C4. Although the overall ΔPA of VG-F is random (Figure 10), the VG-F ΔPA map indicates that the local velocity gradients tend to be more perpendicular to the filaments in the outskirts of this system, and then become more random near the hub center. This may hint that the gas kinematics near the hub center become more complicated, turbulent, or chaotic.

4.4.3. Trends with Intensity

Given the spatial trends identified in the previous section, we now further investigate a possible evolution from the outer area to the hub center. In order to do so, we separate the matched pairs in Figure 9 into a dense-area group ($I > 1000$ mJy beam $^{-1}$) and a diffuse-area group ($I < 1000$ mJy beam $^{-1}$). This boundary is chosen so that filaments in the dense-area group are likely supercritical (see Section 5.1 and Figure 5). The histograms of ΔPA for the two groups are shown in Figure 12, and the distributions of ΔPA versus the local intensity is reported in Appendix B. Since the samples

in the diffuse area are larger than in the dense area, the overall statistics in Figure 9 are dominated by the diffuse samples, and thus, identical trends are found in the isolated diffuse samples in Figure 12. Nevertheless, from the comparison between the low- and high-intensity groups, we find that the interaction between the physical parameters evolves with the local density: The B-F pair evolves from no tendency, i.e., no prevailing alignment ($p=0.732$) in the low-intensity regions to aligned ($p<0.001$) in the high intensity regions. In contrast, the VG-B and VG-G pairs change from prevailing perpendicular ($p=0.008$ and $p=0.021$) in the low-intensity regions to no tendency ($p=0.607$ and $p=0.760$) in the high-intensity regions. *In summary, these findings reveal a tightening alignment between filaments, gravity, and magnetic field with growing intensity, while the local velocity structures become more disordered.*

4.5. Global Stability of G33.92+0.11

In this section, we aim to investigate the global stability of G33.92+0.11 by evaluating the balance between gravity, magnetic field, and gas kinematics. In order to estimate the magnetic field strength from the polarization data, we use both the Davis-Chandrasekhar-Fermi (DCF) method (Davis 1951; Chandrasekhar & Fermi 1953) in Section 4.5.1, and the structure function (SF) method (Houde et al. 2009) in Section 4.5.2. The calculated magnetic energy scale is compared with the gravitational and kinematic energies using the virial theorem in Section 4.5.3.

4.5.1. Davis-Chandrasekhar-Fermi Method

The DCF method assumes that kinematic and magnetic energy are in equipartition. Therefore, the level of magnetic field perturbation (traced by the magnetic field angular dispersion $\delta\phi$) that can result from turbulence (traced by the LOS non-thermal velocity dispersion $\sigma_{v,NT}$) is determined from both the plane-of-sky magnetic field strength (B_{pos}) and the gas volume density ρ by

$$B_{pos} = Q \sqrt{4\pi\rho} \frac{\sigma_{v,NT}}{\delta\phi}, \quad (6)$$

where Q is a factor accounting for complex magnetic field and inhomogeneous density structures. Ostriker et al. (2001) suggested that $Q = 0.5$ yields a good estimation of the magnetic field strength on the plane of sky if the magnetic field angular dispersion is less than 25° .

As the role of the magnetic field may evolve with local density, we separate G33.92+0.11 into three areas with diameters of 1, 3, and 5 FWHM size of the central hub ($30.5''$) as shown in Figure 1. We select the

polarization segments in each area and calculate its polarization angular dispersion. In order to remove a possible bias from an underlying large-scale magnetic field morphology contributing to the dispersion, we calculate differences in polarization angles only using nearest pixel pairs. The polarization angular dispersion is derived as

$$\delta\phi = \sqrt{\frac{1}{N-1} \sum_{i=1}^N \delta PA_i^2}, \quad (7)$$

where δPA is the absolute difference between two polarization angles for every possible nearest-polarization pair, N is the total number of pairs, and the factor $1/(N-1)$ is to debias the population standard deviation estimator. The calculated δPA within the 1, 3, and 5 FWHM areas are listed in Table 1.

To estimate the mean volume densities in the areas, we have first calculated a column density map using the $850 \mu\text{m}$ continuum data assuming a constant dust temperature of 20 K and a dust opacity κ of $0.012 \text{ cm}^2/\text{g}$ (Hildebrand 1983). The total mass of each area is integrated from the column density over the selected area. The mean volume density is then estimated from the total mass and assuming a spherical volume.

In order to estimate the mean non-thermal velocity dispersion, we first average the observed C^{18}O line widths in each area. Assuming a gas kinematic temperature (T_{kin}) of 20 K, the thermal velocity dispersion for C^{18}O is $\sqrt{\frac{k_B T_{\text{kin}}}{m_{\text{C}^{18}\text{O}}}} = 0.09 \pm 0.01 \text{ km s}^{-1}$. The thermal velocity dispersion is then removed from the observed line width to obtain the non-thermal velocity dispersion as

$$\sigma_{v,NT}^2 = \sigma_{obs}^2 - \frac{k_B T_{\text{kin}}}{m_{\text{C}^{18}\text{O}}} \quad (8)$$

where σ_{obs} is the observed C^{18}O Gaussian line width, and $m_{\text{C}^{18}\text{O}}$ is the molecular weight. The resulting magnetic field strengths for the three areas are listed in Table 1.

4.5.2. Structure Function Method

Houde et al. (2009) expanded the DCF method, assuming that the magnetic field is composed of an ordered large-scale component (B_0) and a turbulent component (B_t). The ratio of these two components determines the polarization angular dispersion as

$$\delta\phi = \left[\frac{\langle B_t^2 \rangle}{\langle B_0^2 \rangle} \right]^{\frac{1}{2}}, \quad (9)$$

where $\langle \dots \rangle$ denotes an average. Hence, the DCF equation (Equation 6) can be rewritten as

$$B_{pos} = \sqrt{4\pi\rho} \sigma_{v,NT} \left[\frac{\langle B_t^2 \rangle}{\langle B_0^2 \rangle} \right]^{-\frac{1}{2}}, \quad (10)$$

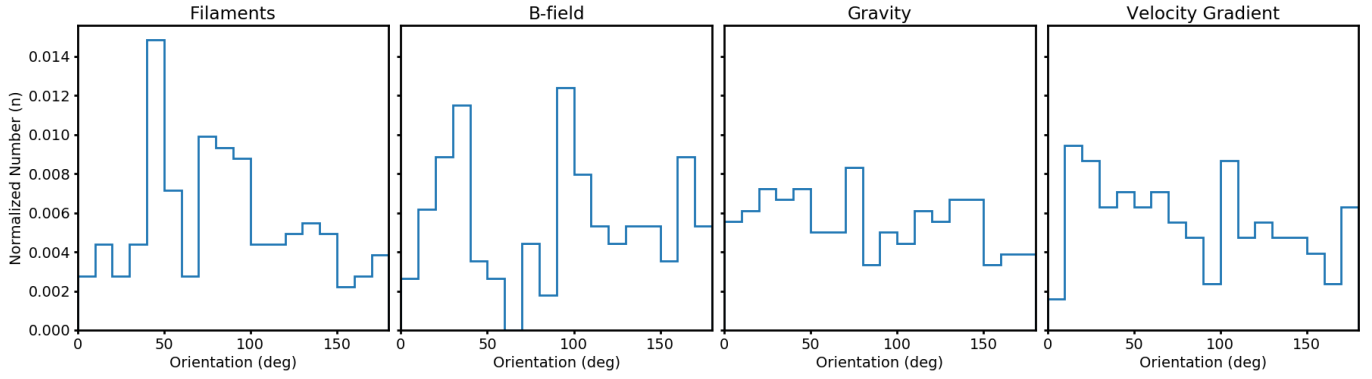


Figure 8. Normalized histograms of local orientations of filaments, magnetic field, gravity, and velocity gradients. The position angle is defined following the IAU standard, $PA=0^\circ$ referring to north and increasing counterclockwise to east.

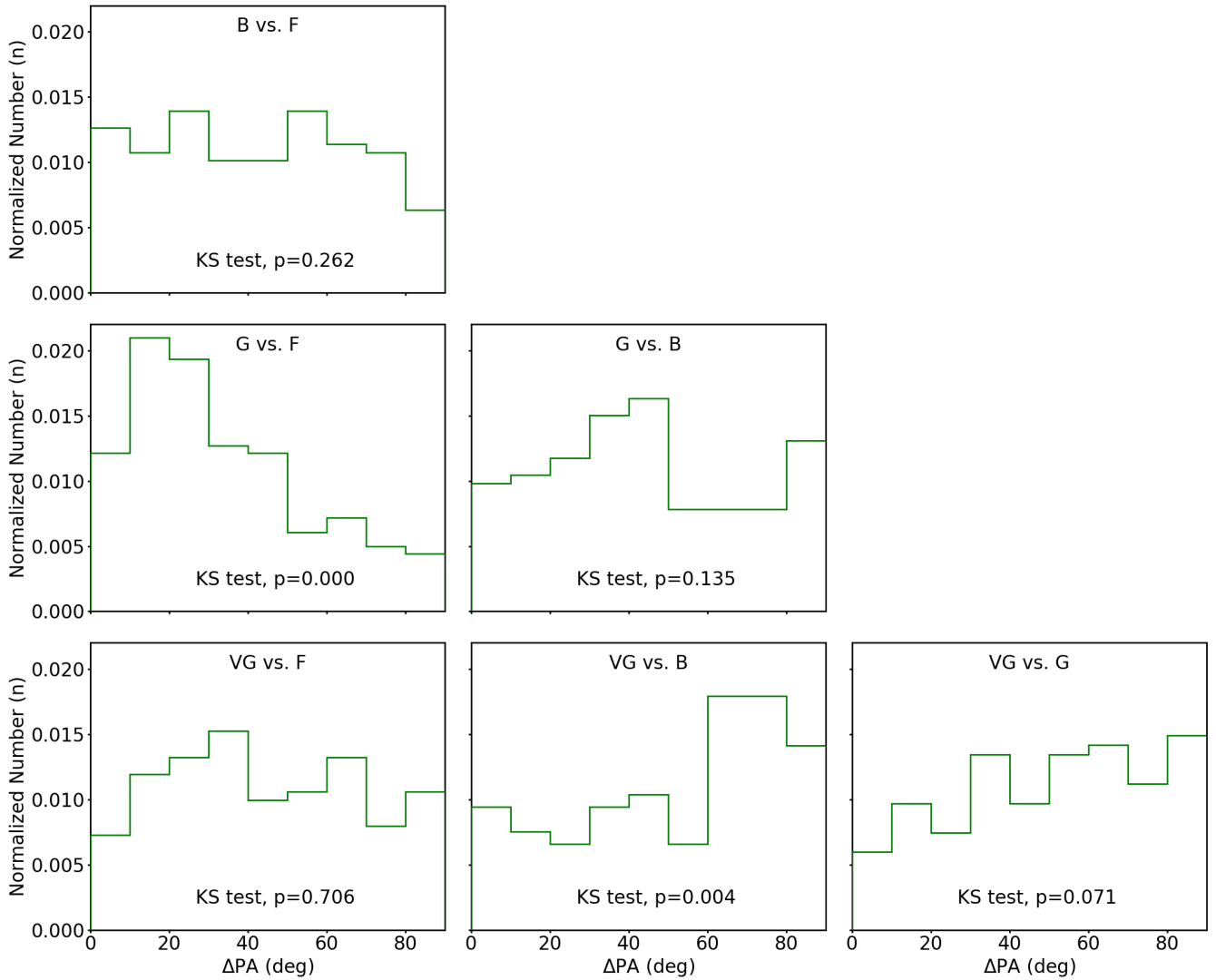


Figure 9. Normalized histograms of local pair-wise differential orientations among filaments, magnetic field, gravity, and velocity gradients. p-values from KS tests are given in each panel.

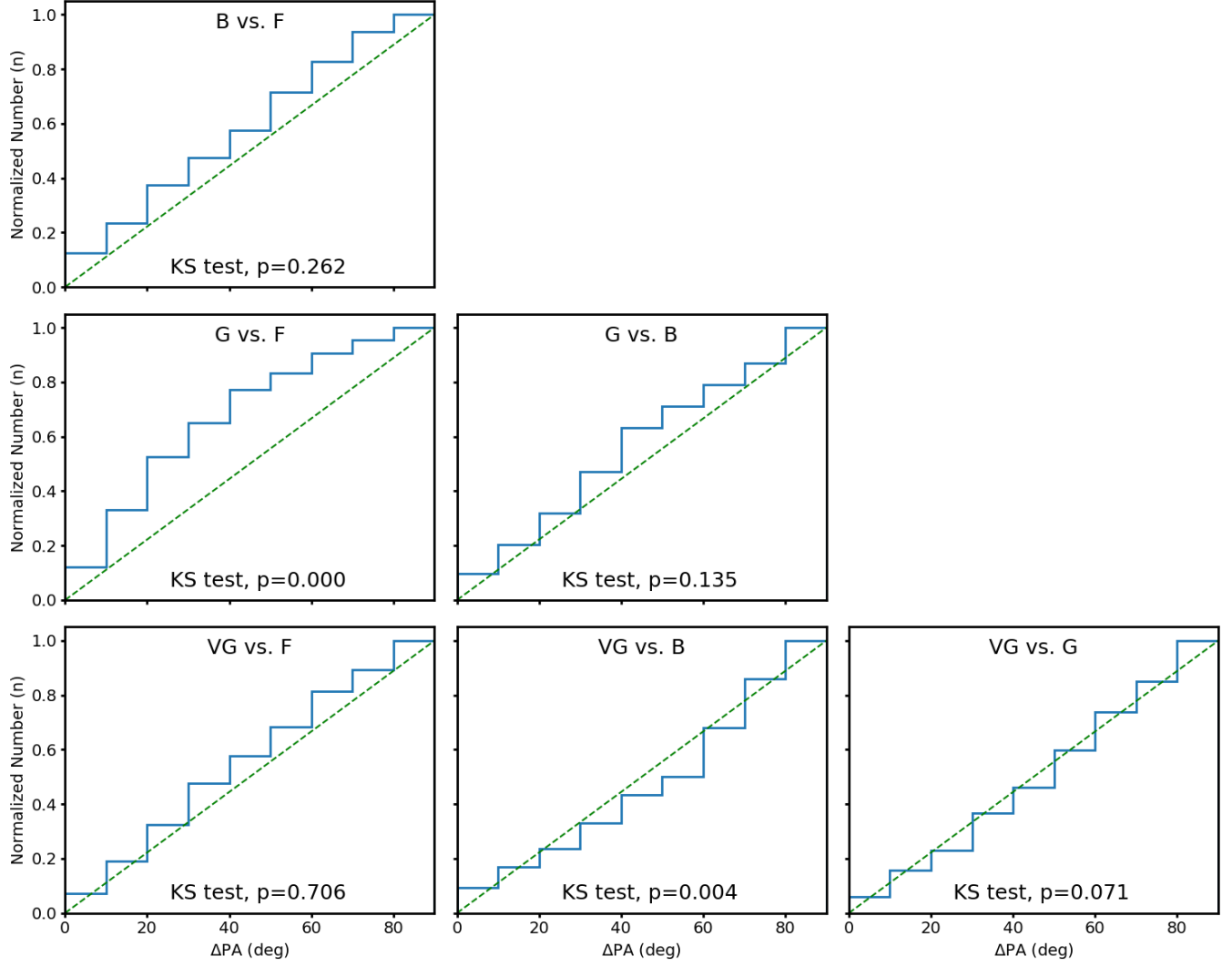


Figure 10. Cumulative distributions of differential orientations among the associated filaments, magnetic field, gravity, and velocity gradients, based on Figure 9. The green dashed diagonal line indicates the random distribution. The resulting p-values of the KS-tests are given in each panel. The G vs F distribution can be classified as parallel-like while the VG vs B distribution is perpendicular-like. A threshold of $p < 0.05$ is adopted as a non-random distribution with a 95% confidence interval.

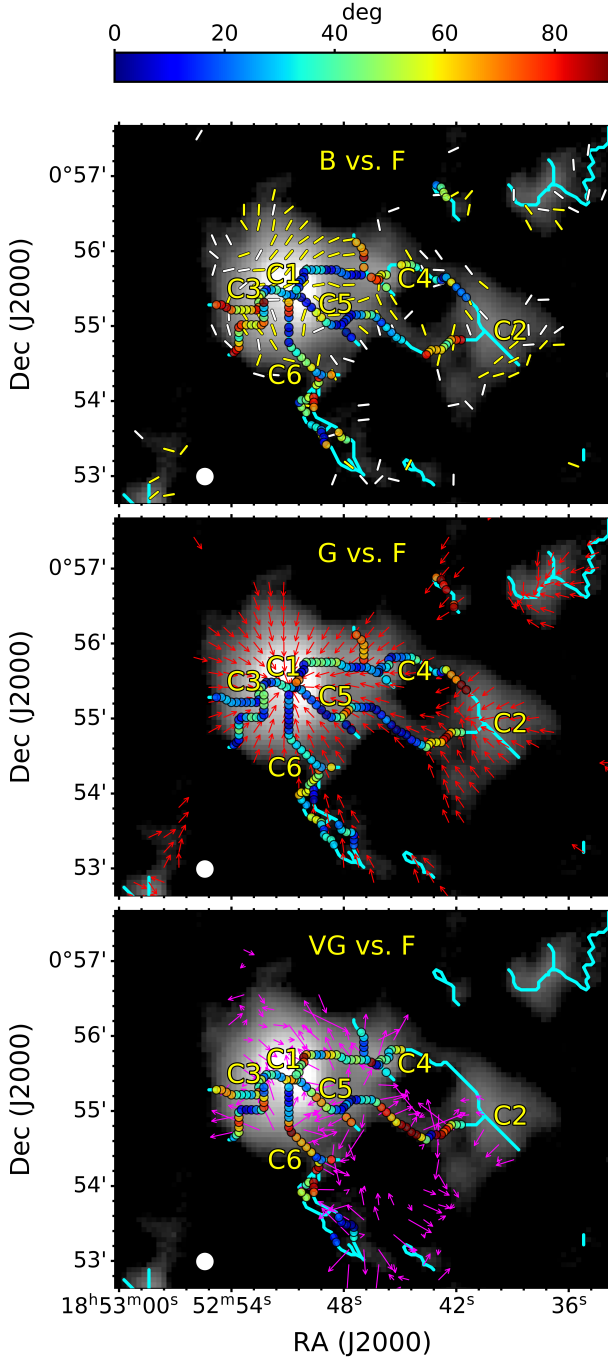


Figure 11. Differential orientation maps for filament vs magnetic field, gravity, and velocity gradient (from top to bottom), overlaid on the $850 \mu\text{m}$ intensity. The cyan lines are the filaments identified in Figure 3. The yellow and white segments represent the magnetic field orientations from Figure 1, the red arrows are the projected local gravity, and the magenta arrows show the local velocity gradients. Filled color-coded circles (color wedge) are the pairwise differential orientations ΔPA .

where the original correction factor Q in the DCF equation is neglected, because the structure function approach is expected to remedy the possible bias originating from the depolarization effect due to the turbulent magnetic field component. Houde et al. (2009) further showed that the ratio of turbulent-to-magnetic energy can be estimated from the structure function using the following equation:

$$1 - \langle \cos[\Delta\Phi(\ell)] \rangle \simeq \frac{1}{N} \frac{\langle B_t^2 \rangle}{\langle B_0^2 \rangle} (1 - e^{-\ell^2/2(\delta^2 + 2W^2)}) + a\ell^2, \quad (11)$$

where $\Delta\Phi(\ell)$ is the structure function that describes the difference between polarization angles separated by a distance ℓ . δ and a are unknown parameters, representing the turbulent correlation length and the first order Taylor expansion of the large-scale magnetic field structure. W is the telescope beam radius, which is $6''.2$ at $850 \mu\text{m}$ for the JCMT. N is the number of turbulent cells along the line of sight and within the telescope beam, and can be estimated from:

$$N = \Delta' \frac{\delta^2 + 2W^2}{\sqrt{2\pi}\delta^3}, \quad (12)$$

where Δ' is the effective cloud thickness. Fitting the above equation to the observed $1 - \langle \cos[\Delta\Phi(\ell)] \rangle$ vs ℓ distribution yields the three unknown parameters δ , $\frac{\langle B_t^2 \rangle}{\langle B_0^2 \rangle}$, and a .

Identical to the three areas defined for the DCF method, we calculate three separate dispersion functions. The derived $\cos[\Delta\Phi(\ell)]$ are averaged in bins of $12''$. The resulting angular dispersion functions with their best fits of Equation 11 are plotted in Figure 13. The fitting parameters are given in Table 1. We note that no fit is attempted for the 1 FWHM area because this small area only yields three binned $\cos[\Delta\Phi(\ell)]$ values. Generally, the magnetic field strengths estimated from the DCF method are larger than the ones from the SF method by a factor of ~ 1.5 . A possible reason for this discrepancy is that the observed $\delta\Phi$ are beyond the reliable range ($< 25^\circ$) for the DCF method as suggested by Ostriker et al. (2001).

To evaluate the relative importance between magnetic field and gravity, the mass-to-flux ratio (λ_{obs}) is calculated as

$$\lambda_{obs} = 2\pi\sqrt{G} \frac{\mu m_H N_{H_2}}{B_{pos}}, \quad (13)$$

where $\mu=2.33$ is the mean molecular weight per H_2 molecule (Nakano & Nakamura 1978). Due to the unknown inclination, the observed mass-to-flux ratio λ_{obs} is only an upper limit. Crutcher et al. (2004) suggest that a statistical average factor of $1/3$ can be used to

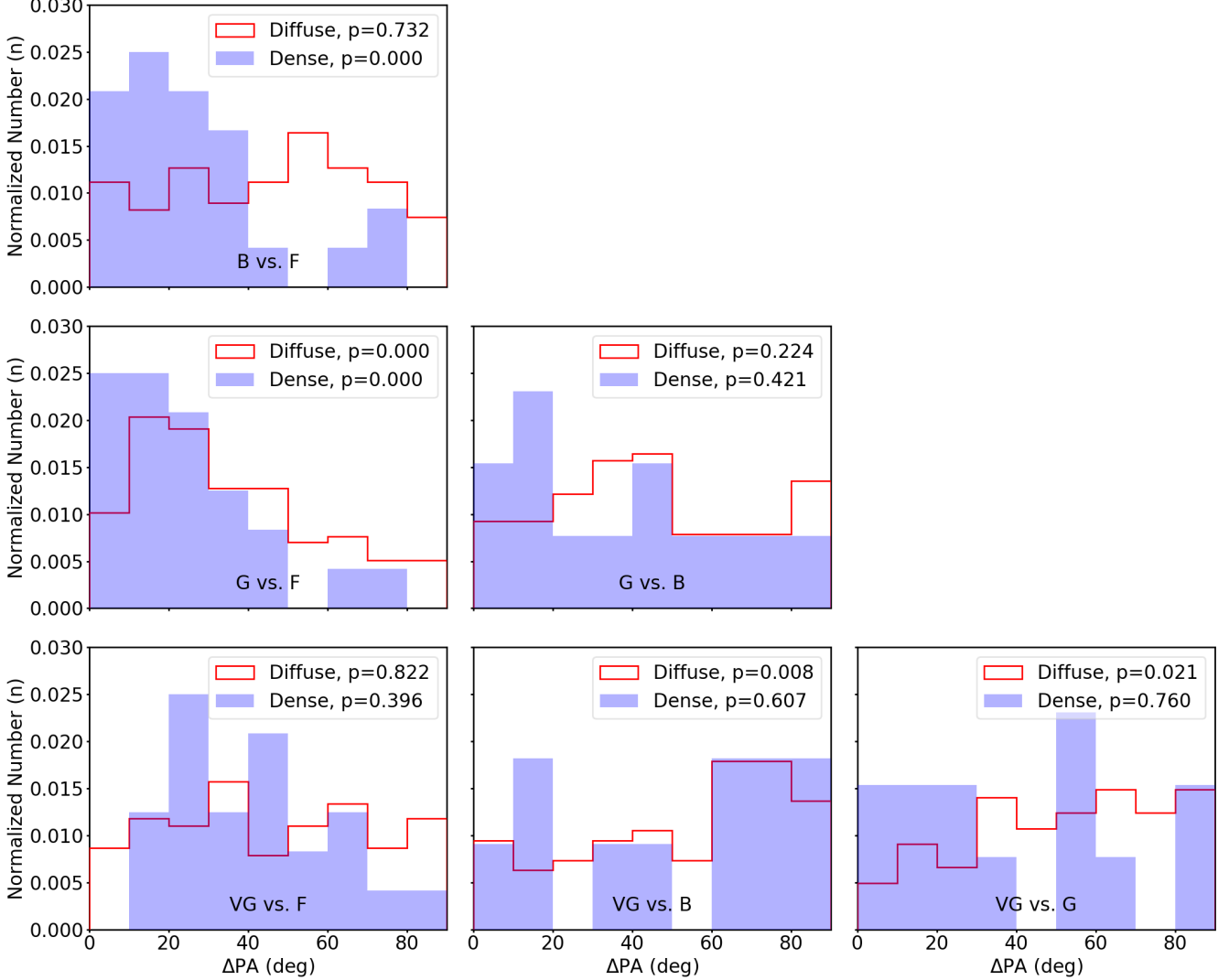


Figure 12. Normalized histograms of the pairwise differential orientations between filaments, magnetic field, gravity, and velocity gradients, for two different intensity ranges. The blue and red histograms represent the ΔPA selected in the dense ($I_{850} > 1000 \text{ mJy beam}^{-1}$) and the diffuse ($I_{850} < 1000 \text{ mJy beam}^{-1}$) areas. The KS-test results against the random distribution are listed for the two areas.

better estimate the mass-to-flux ratio accounting for the random inclinations in a sample of oblate spheroid cores, flattened perpendicular to the magnetic field. Thus, the corrected mass-to-flux ratio (λ) becomes

$$\lambda = \frac{\lambda_{obs}}{3}. \quad (14)$$

We note that this correction factor is determined from the cloud and magnetic field geometry. A correction factor of $\pi/4$ is suggested for a spherical cloud (Crutcher et al. 2004), and a factor of $3/4$ for a prolate spheroid elongated along the magnetic field (Planck Collaboration et al. 2016). Using a correction factor of $1/3$, the estimated mass-to-flux ratios (2–3) are larger than unity for all areas. This suggests that this HFS is supercriti-

cal. The mass-to-flux ratios would be even more supercritical if other correction factors were used, and they would only become subcritical if the magnetic fields were nearly along the line-of-sight. A globally supercritical condition is in agreement with the overall converging filamentary structures aligned with gravity and the growing density along these filaments, because these features require dominating gravity driving mass to the center.

4.5.3. Virial Balance

The virial theorem is commonly used to analyze the balance between gravitational, magnetic, and kinematic energy in a molecular cloud. In Lagrangian form it can

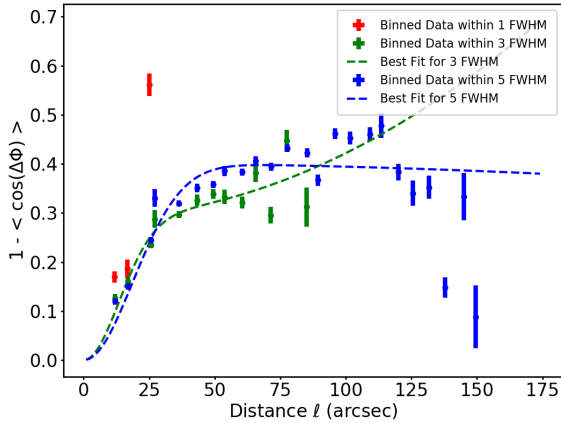


Figure 13. Structure functions for polarization data selected within 1, 3, and 5 FWHM areas. The dashed lines show the best fits following Equation 11.

be written as

$$\frac{1}{2}\ddot{I} = 2(\mathcal{T} - \mathcal{T}_s) + \mathcal{M} + \mathcal{W}, \quad (15)$$

(e.g., Mestel & Spitzer 1956; McKee & Ostriker 2007) where I is a quantity proportional to the trace of the inertia tensor of the cloud. The sign of \ddot{I} determines the acceleration of the expansion or contraction of the cloud. The term

$$\mathcal{T} = \frac{3}{2}M\sigma_{obs}^2 \quad (16)$$

is the total kinematic energy, where M is the total mass and σ_{obs} is the observed total velocity dispersion. We neglect the surface kinetic term \mathcal{T}_s because we aim at estimating the self-stability of an enclosed region. Nevertheless, we note that the presence of any external pressure could suppress gravitational support and enhance the cloud’s instability. The magnetic energy term, without any force from an external magnetic field, is

$$\mathcal{M} = \frac{1}{2}MV_A^2, \quad (17)$$

where $V_A = B/\sqrt{4\pi\rho}$ is the Alfvén velocity and ρ is the mean density. We note that the magnetic field morphology is not accounted for in this magnetic energy term. As the DCF and SF method only constrain the plane-of-sky magnetic field component, we use the statistical average to correct and estimate the total magnetic field strength as $B = (4/\pi)B_{pos}$ (Crutcher et al. 2004). The term

$$\mathcal{W} = -\frac{3}{5}\frac{GM^2}{R} \quad (18)$$

is the gravitational potential of a sphere with a uniform density ρ and a radius R .

We derive the ratios of $|\mathcal{T}/\mathcal{W}|$ and $|\mathcal{M}/\mathcal{W}|$ in Table 1 for the three selected areas to evaluate the relative importance among kinematic, magnetic, and gravitational energy. The estimated energy scales generally indicate a relative importance of $|\mathcal{W}| > |\mathcal{T}| \gtrsim |\mathcal{M}|$, suggesting that gravity overall dominates the system. The kinematic energy is comparable to the magnetic energy, as $|\mathcal{T}/\mathcal{W}|$ is only larger than $|\mathcal{M}/\mathcal{W}|$ by a factor of 1.2–2.5. The relative importance of these three parameters is similar in the three selected areas, although the relative importance of kinematic energy seems to slightly increase near the central area.

As \mathcal{T} and \mathcal{M} are positive and \mathcal{W} is negative, the sign of \ddot{I} in Equation 15 is positive (expanding) if $|\frac{2\mathcal{T}+\mathcal{M}}{\mathcal{W}}| > 1$ or negative (contracting) if $|\frac{2\mathcal{T}+\mathcal{M}}{\mathcal{W}}| < 1$. All the derived values for $|\frac{2\mathcal{T}+\mathcal{M}}{\mathcal{W}}|$ are lower than unity, suggesting that the kinematic and magnetic energy cannot support the system, and hence the whole system is contracting globally.

5. DISCUSSION

5.1. Filament Properties

Herschel observations suggest that filamentary structures are ubiquitous in molecular clouds, and are likely progenitors of star formation. These filaments have widths within a narrow range around ~ 0.1 pc, and tend to be co-linear in direction to the longer extents of their host clouds (André et al. 2014). Using the same DisPerSe algorithm, we have identified numerous filaments within the G33.92+0.11 HFS. The identified filaments show an overall converging configuration where all filaments are connecting to the massive central hub. This configuration is consistent with other known HFS, e.g., G10.6-0.4 (Liu et al. 2012b), W49 (Galván-Madrid et al. 2013), B59 (Peretto et al. 2012) and SDC13 (Williams et al. 2018), but different from other filamentary systems with co-linear orientations, e.g., IC5146 (Arzoumanian et al. 2011) and B211/213 (Palmeirim et al. 2013).

In addition to the overall configuration, we have measured the width and the peak intensity along the identified filaments. The derived median deconvolved FWHM is 0.5 pc, which is larger than the common filament width of 0.09 ± 0.07 pc in the *Herschel* samples by a factor of 5 (Arzoumanian et al. 2011; André et al. 2014; Arzoumanian et al. 2019). We further find that the filament widths grow with the ridge intensity from 0.5–0.7 pc until the intensity reaches ~ 1000 mJy beam $^{-1}$, and then turn to decrease to 0.5 pc as the intensity further increases.

The variation in filament widths has been seen in models studying the evolution of externally pressurized filaments (Fischera & Martin 2012; Heitsch 2013a,b). In

Table 1. Parameters for Magnetic Field Strength Estimates and Virial Analysis.

Regions	$\frac{\langle B_t^2 \rangle}{\langle B_0^2 \rangle}$	δ	$\sigma_{v,NT}$	$\delta\phi^b$	n_{H_2}	B_{pos}	λ	$ \frac{\mathcal{T}}{\mathcal{W}} $	$ \frac{\mathcal{M}}{\mathcal{W}} $	$ \frac{2\mathcal{T}+\mathcal{M}}{\mathcal{W}} $
		pc	(km s ⁻¹)	(deg)	(cm ⁻³)	(μ G)				
DCF method										
1 FWHM sphere	1.5 \pm 0.1 ^a	...	1.3 \pm 0.1	35.2 \pm 1.3	(1.0 \pm 0.1) \times 10 ⁵	230 \pm 8	2.0 \pm 0.1	0.17 \pm 0.01	0.08 \pm 0.01	0.42 \pm 0.01
3 FWHM sphere	1.1 \pm 0.1 ^a	...	1.1 \pm 0.1	30.0 \pm 1.2	(1.0 \pm 0.1) \times 10 ⁴	74 \pm 3	1.8 \pm 0.1	0.15 \pm 0.01	0.10 \pm 0.01	0.41 \pm 0.01
5 FWHM sphere	1.0 \pm 0.1 ^a	...	0.8 \pm 0.1	29.3 \pm 1.9	(2.5 \pm 0.3) \times 10 ³	27 \pm 2	2.1 \pm 0.1	0.10 \pm 0.01	0.08 \pm 0.01	0.29 \pm 0.01
SF method										
3 FWHM sphere	1.85 \pm 0.63	0.35 \pm 0.06	1.1 \pm 0.1	...	(1.0 \pm 0.1) \times 10 ⁴	57 \pm 10	2.3 \pm 0.4	0.15 \pm 0.01	0.06 \pm 0.01	0.36 \pm 0.01
5 FWHM sphere	1.90 \pm 0.3	0.57 \pm 0.06	0.8 \pm 0.1	...	(2.5 \pm 0.3) \times 10 ³	20 \pm 2	2.8 \pm 0.3	0.10 \pm 0.01	0.04 \pm 0.01	0.25 \pm 0.01

NOTE— δ , $\sigma_{v,NT}$, $\delta\phi$, n_{H_2} , B_{pos} , λ , \mathcal{T} , \mathcal{M} , and \mathcal{W} are the turbulence length scale, non-thermal velocity dispersion, magnetic field angular dispersion, H₂ volume density, plane-of-sky magnetic field strength, mass-to-flux ratio, kinematic energy (both thermal and non-thermal), magnetic energy, and gravitational energy, respectively.

^aThe ratio of turbulent-to-large-scale magnetic field components is estimated assuming $[\frac{B_t}{B_0}]^2 = \frac{\delta\phi^2}{Q}$.

^bThe angular dispersion is estimated from pairs of polarization segment separated by 14'', which is the smallest physical scale we can probe.

these models, the internal gas motion is driven by the accretion onto filaments. Consequently, the turbulent pressure grows as the filaments gain mass. This is consistent with the observed increase in velocity dispersion with peak intensity (right panel in Figure 2). If the internal turbulent pressure grows faster than gravity and any external pressure, the excess gas pressure will expand the filaments until the gas pressure is balanced again by gravity. On the other hand, once sufficient mass has been accreted, the filament becomes super-critical and starts to contract, causing a turnover and eventually leading to a decreasing radius. These mechanisms result in a peaked dependence on filament width and column density, and the peak will be around 0.5–2 times the critical linear density, depending on the filament’s inclination angle.

In order to show that the observed variation in filament widths is consistent with the models described above, we have calculated the critical linear density as follows. Considering the support of both thermal and non-thermal gas motion⁵, the critical linear density is $M_{line,critical} = 2(c_s^2 + \sigma_{v,NT}^2)/G$ (Fiege & Pudritz 2000). As the observed C¹⁸O velocity dispersion is 0.05 km s⁻¹

⁵ The term “non-thermal motion” refers to the motion traced by the observed non-thermal velocity dispersion, which includes turbulence but possibly also line-of-sight components of infall and rotational motion. In massive star-forming regions, gravitationally driven infall and rotational motion can be one of the major components in the observed non-thermal velocity dispersion (e.g., Heyer et al. 2009; Traficante et al. 2020). The kinematic energy in the virial analysis is, therefore, also derived with both the thermal and non-thermal component.

in the diffuse area, dominated by the thermal motion, the critical linear density is dominated by the c_s term, which is ~ 0.2 km s⁻¹ for a mean molecular weight of 2.33 at 20 K. In contrast to that, the observed velocity dispersion is ~ 1.2 km s⁻¹ in the central hub, dominated by the non-thermal motion $\sigma_{v,NT}$ term. This results in an increase of the $M_{line,critical}$ from $\sim 20M_\odot/pc$ in the diffuse area to $\sim 800M_\odot/pc$ in the dense area.

Additionally to the above estimated support, magnetic fields can play a role in stabilizing filaments. However, the exact magnetic support is determined by the morphology of the magnetic field within a filament, for which our current data do not have sufficient resolution. The general virial analysis for magnetized filaments shows that poloidal-dominated fields help supporting filaments against gravity while toroidal-dominated fields destabilize filaments (Fiege & Pudritz 2000). The critical linear density of a magnetized filament is $M_{line,vir}^{mag} = M_{line,critical} \times (1 - \mathcal{M}/\mathcal{W})^{-1}$, where \mathcal{M} is the magnetic energy per unit length (positive for poloidal fields and negative for toroidal fields) and \mathcal{W} is the gravitational energy per unit length. To estimate the upper and lower limit of $M_{line,vir}^{mag}$, we adopt our estimated $|\frac{\mathcal{M}}{\mathcal{W}}| \sim 0.08$ (Table 1). $(1 \pm \mathcal{M}/\mathcal{W})^{-1}$ then yields 0.9 (purely toroidal) and 1.1 (purely poloidal). Hence, the $M_{line,vir}^{mag}$ is estimated to be ~ 700 – $900 M_\odot/pc$, corresponding to a H₂ column density of 4 – 5×10^{22} cm⁻² for a filament width of 0.7 pc and an 850 μ m intensity of ~ 530 – 660 mJy/beam assuming a dust temperature of 20 K.

This estimated critical linear density (highlighted in Figure 5 as a green shaded region) is within the intensity range of $\sim 500\text{--}1000$ mJy beam $^{-1}$ where the maximum filament widths occur. *We, therefore, conclude that the observed trend and change in filament widths are consistent with the predictions of externally pressurized filament models. Due to the support from the non-thermal kinematic energy, most of the filaments in G33.92+0.11 remain subcritical until entering the massive center area with a radius of ~ 1 pc (third contour in Figure 1).* We speculate that this additional support from non-thermal energy is one of the reasons why these filaments can transfer a significant amount of mass toward the center hub before self-fragmenting and forming massive clusters.

The filaments within G33.92+0.11 may not be the same type of filaments as identified by *Herschel* (e.g., André et al. 2010; Arzoumanian et al. 2011). The statistical analysis based on 599 filaments from the *Herschel* Gould Belt survey (Arzoumanian et al. 2019) shows that most of the filaments have a central column density ranging from 5×10^{20} to 2×10^{22} cm $^{-2}$, and the central column densities within the same filament are typically comparable. In contrast, several filaments in G33.92+0.11 show a variation in peak intensity of one or even two orders of magnitude. In addition, the dense filaments in G33.92+0.11 can reach a density of $\sim 10^{23}$ cm $^{-2}$. Such massive examples are rare in the *Herschel* Gould Belt survey samples. Arzoumanian et al. (2013) measured the velocity dispersion of the filaments identified by *Herschel* in IC5146, Aquila, and Polaris, and found that these filaments have total velocity dispersions of 0.2–0.6 km s $^{-1}$, which is less than half of the peak velocity dispersion seen in G33.92+0.11. As the strong turbulent pressure can significantly increase the critical linear density for the filaments in G33.92+0.11 – by a factor of ~ 40 compared to the *Herschel* filaments – the filaments in G33.92+0.11 are able to accrete and transfer a large amount of mass to the center before self-fragmenting and forming massive clusters.

5.2. Origin of Local LOS Velocity Gradient

The statistics in Section 4.4 show that local gravity tends to be parallel to filaments (Figure 12). Since the observed velocity gradients tend to be perpendicular to local gravity in the diffuse areas (Figure 12), one might expect the local velocity gradients to also be perpendicular to filaments. The bottom panel in Figure 11 illustrates that the local velocity gradients in the diffuse areas tend to be perpendicular to the long major filaments that connect to the center hub (C1), except for the regions near the minor converging points (C3, C4,

and C5). The minor filaments that connect to the minor converging points appear to be aligned with the local velocity gradients. Thus, the filament-velocity gradient statistics are biased by a mixture of major and minor filaments. Based on the map displaying spatial tendencies, we conclude that local velocity gradients in the diffuse areas are still significantly tied to filaments: they are perpendicular to major filaments, but parallel to minor filaments.

The above trend is similar to the filament-striation configuration in the Taurus B211/213 system. The ^{12}CO and ^{13}CO line observations in Goldsmith et al. (2008) reveal numerous fine and diffuse filamentary structures, named striations, perpendicular to the major filamentary cloud but parallel to local magnetic fields. Palmeirim et al. (2013) further describe a significant velocity gradient parallel to the striations but perpendicular to the major filament. Shimajiri et al. (2019) model these velocity structures and suggest that the striations represent mass accretion from the ambient cloud to the major filaments along the magnetic field. This magnetic-field-guided mass accumulation has also been seen in other filamentary systems, such as Serpens South (Fernández-López et al. 2014; Chen et al. 2020a), Musca (Cox et al. 2016) and G34.43+00.24 (Tang et al. 2019).

One major difference between G33.92+0.11 and the filament-striation systems is that the local velocity gradients in G33.92+0.11 tend to be perpendicular to, instead of following the magnetic fields (Figure 12). Magnetic fields parallel to striations but perpendicular to major filaments are expected to be a feature of systems with strong magnetic fields (e.g., Shu et al. 1987; Nakamura & Li 2008). In such systems, magnetic fields regulate the collapse of a cloud, and thus guide the accretion flow toward major filaments (Nakamura & Li 2008). However, a magnetic-field-regulated collapse is not the only mechanism that can produce accretion flows perpendicular to a filament. Simulations of filaments produced by colliding turbulent flows can also explain the observed local velocity gradients perpendicular to filaments because the material surrounding the filaments tends to collapse parallel to the shock-compressed layers (Gong & Ostriker 2011; Gómez & Vázquez-Semadeni 2014; Chen et al. 2020a). In this scenario, minor converging points are intersections of multiple accretion flows, where they merge and are redirected toward a major converging point. This might explain the observed alignment between filaments and local velocity gradients around the minor converging points because here the gas kinematics are dominated by filaments merging due to local gravity instead of accumulating surrounding ambient mass. This scenario seems to better explain the

observed trend of local velocity gradients being perpendicular to local magnetic fields. Moreover, this scenario is also supported by the estimated relatively weak magnetic energy.

The spatial resolution of our polarization observations can only marginally resolve the filaments. Hence, we cannot completely exclude the possibility that the magnetic field outside the filaments is actually more parallel to the velocity gradient, but the observation is dominated by the polarization inside the filaments, where the magnetic field becomes parallel to the filament axis. Nevertheless, such a turn-over magnetic field morphology is also a feature predicted by turbulent compression models (Padoan et al. 2001a; Chen & Ostriker 2014, 2015; Gómez et al. 2018). This is because the magnetic fields perpendicular to filaments on large scales, might be either bent by shocked gas layers or pinched by gas motions along filaments, and thus become parallel to filaments near a ridge. This has recently been seen in NGC6334 (Arzoumanian et al. 2020). Hence, even when considering the possibly unresolved turn-over magnetic field morphology, the observed magnetic fields perpendicular to local velocity gradients still favor a turbulent compression scenario. Finally, we note that our analysis is only based on the LOS velocity component, and a significant plane-of-sky velocity component might change this picture.

5.3. *Velocity Gradient Magnitude and Velocity Dispersion*

In addition to the direction of the LOS velocity gradient, we find that the magnitude of the velocity gradient decreases from the outer area to the central hub (Figure 14). Since the differential orientations between filaments and local velocity gradient tend to be overall random, the local velocity gradient components (parallel and perpendicular to filaments) both also decrease in magnitude towards the central hub. In addition, we further find that the LOS velocity dispersion increases while the local velocity gradient magnitude decreases, as illustrated in Figure 15.

The opposite trend between local velocity gradient magnitude and velocity dispersion may suggest a change in the velocity power spectrum. It is known that turbulence and the correlated gas kinematics are scale-dependent in molecular clouds, as described by Larson’s law (e.g., Larson 1981; McKee & Ostriker 2007). Observationally, LOS velocity gradients are often calculated from LOS velocities measured at pixels with particular separations, usually the beam size. Adopting a centroid velocity only traces the velocity of the densest component along the line of sight, but lacks the information

of velocity variation along the line of sight. Hence, a resulting velocity gradient is only sensitive to the gas kinematics at a scale comparable to the physical distance between these densest components of the selected pixels. Since G33.92+0.11 is likely a face-on system (Liu et al. 2012a), the physical distance is approximately the plane-of-sky distance. Hence, the estimated local velocity gradients are sensitive to gas motions on a ~ 0.5 pc scale. In contrast, the observed velocity dispersion includes velocity information of all components at all physical scales along the line of sight.

An increase in velocity dispersion towards high-density regions has been observed in the HFS SDC13 (Williams et al. 2018). Since turbulent energy is expected to dissipate in stagnation regions generated by shock compression, contrary to the observed trends (Figure 15), the growing velocity dispersion more likely originates from gravity instead of turbulence. Li & Klein (2019) have simulated the formation of filaments in a magnetized cloud driven by turbulence and self-gravity. Their velocity power spectra reveal an increase in power at small scales ($\lesssim 0.1$ pc) after gravity is turned on. Self-gravity also causes growing power of density structures at a $\lesssim 0.5$ pc scale. If observed in low resolution ($\gtrsim 0.5$ pc), this subparsec-scale processes could result in an increase in velocity dispersion, as seen in SDC13 and also here in G33.92+0.11.

The high-resolution SMA and ALMA molecular line observations reveal that the inner 0.5 pc area of the G33.92+0.11 central hub is fragmented into several young clusters surrounded by four converging spiral-arm-like structures (Liu et al. 2012a, 2015). About 30 young stellar objects are identified within these clusters (Liu et al. 2019). These structures suggest that local gravitational fragmentation has taken place within the central hub of G33.92+0.11. These 0.01-pc scale fragmentation process is similar to the Li & Klein (2019) model, and hence might explain the increase in velocity dispersion seen with our resolution (0.5 pc). In addition, the observed spiral-arm-like morphology and the related virial analysis suggest that the rotational energy is important in supporting these 0.1 pc scale structures (Liu et al. 2019). The accelerated rotational motion near the hub center, due to the conservation of angular momentum, could then also contribute to the increase in velocity dispersion. Furthermore, as the central hub of G33.92+0.11 hosts an ultracompact HII region, the feedback from the massive star formation may further enhance the turbulence within the hub, which has been seen in Liu et al. (2012a, 2019).

A decreasing velocity gradient magnitude towards high-density regions is rarely seen in other systems. The

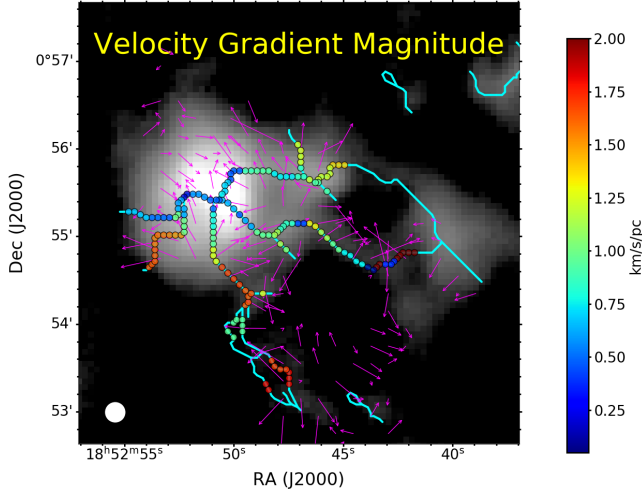


Figure 14. Magnitude of local LOS velocity gradient along filaments overlaid on the JCMT 850 μm continuum map. The velocity gradient magnitude is higher ($\sim 1\text{--}2$ km/s/pc) in the outer area and decreases to ~ 0.5 km/s/pc near the hub center.

opposite trend has been seen in a few systems, such as S242 (Yuan et al. 2020), Mon R2 (Treviño-Morales et al. 2019), and two of the filaments in SDC13 (Williams et al. 2018). On the other hand, a constant velocity gradient magnitude, independent of local density, has also been observed, such as in G35.39 (Sokolov et al. 2019) and the other two filaments in SDC13 (Williams et al. 2018). An increased velocity gradient magnitude toward high-density regions is expected for accretion flows due to gravitational acceleration (e.g., Treviño-Morales et al. 2019), while an opposite trend can likely be related to the gas dynamics originating from large-scale turbulence (e.g., the turbulent fragmentation). This is because large-scale turbulence is expected to dissipate in the high-density stagnation regions. It is still unclear which trend is more common, as the variation of local velocity gradient magnitudes has only been studied in a few systems. To make matters more complicated, the current observations have been probing the velocity gradient at different physical scales, due to the different tracers, angular resolutions, and object distances. A larger and more homogeneous sample with multi-scale velocity gradient measurements is still needed to understand the origin of the magnitude variations.

5.4. Origin of the HFS

Our virial analysis, accounting for the global energy balance of G33.92+0.11, shows that the gravitational energy overall dominates the kinematic and magnetic energy in this system, and hence the whole system is expected to contract. Locally, we find that the filament orientations tend to be aligned with local gravity. This

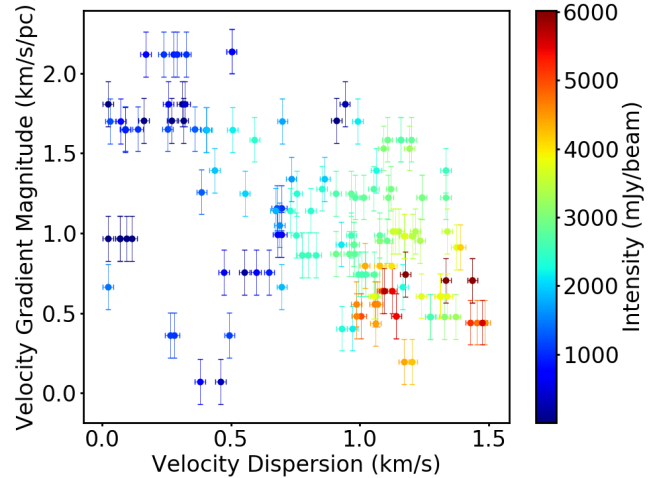


Figure 15. Magnitude of local LOS velocity gradient versus LOS velocity dispersion. Color-coded is the 850 μm intensity. A higher intensity indicates regions closer to the hub center. As the intensity increases, the velocity gradient magnitude decreases while the velocity dispersion increases.

suggests that these filaments are likely accretion streams driven by gravity. In addition to the global contraction, the local velocity gradients reveal gas motions perpendicular to the major filaments in the diffuse areas, hinting that these filaments possibly accumulate ambient gas from the diffuse surrounding while also flowing toward the hub center.

The role of the magnetic field is relatively less important in this system, as compared to gravity and turbulence. In the dense regions, both filaments and magnetic fields are aligned with the gravitational force. Hence the magnetic tension force cannot retard the accretion streams effectively, although it can still help to stabilize the filaments against radial collapse by increasing the critical linear density. In the diffuse regions, magnetic fields still tend to be aligned with the major filaments, but perpendicular to those minor filaments merging into the major filaments. This suggests that magnetic fields might be important in delaying the mass accumulation onto the major filaments. Hence, the density growth rate of the major filaments is less than their turbulence growth rate. Consequently, the turbulent pressure might keep supporting the major filaments from radial collapse until approaching the center. This can then result in a massive protocluster forming in the hub center, instead of numerous young stars randomly distributed over the system. Our interpretation based on all the observed features is schematically illustrated in Figure 16.

This interpretation provides a possible explanation to the question of how massive stars/clusters form in a globally subvirial ($5\sigma_v^2 R / (GM) < 2$) cloud, where the

turbulence pressure is insufficient to support the cloud against gravity, and the cloud is, therefore, expected to fragment to form numerous lower-mass stars before accumulating sufficient mass for massive star formation (McKee & Tan 2003). Kauffmann et al. (2013) argue that the additional support from magnetic fields might stabilize such subvirial clouds and enable massive star formation. However, our virial analysis shows that both magnetic and kinematic energy are insufficient to globally support G33.92+0.11 against gravity, but yet massive star formation is still present. Our analysis further shows that a *globally* unstable system might still host *locally* stable filaments, through which mass can converge toward the center – without fragmenting into low-mass clumps – and enable massive star formation. These findings illustrate the importance of jointly studying global and local properties in order to understand such systems.

Our findings favor the multi-scale gravitational collapse cloud model in Gómez & Vázquez-Semadeni (2014). In this model, a super-Jeans cloud forms from colliding flows and rapidly begins to undergo gravitational collapse. The collapse soon becomes nearly pressureless, proceeding along its shortest dimension, and forms filamentary sub-structures. The resulting filaments are not in a static equilibrium but are long-lived flow structures that accumulate ambient gas from their environment and direct it towards the major gravitational potential well (hub center). This model is based on the physical condition that both thermal and turbulent pressure of the forming cloud are insufficient to stabilize the cloud against gravitational collapse. This is consistent with our estimated gravitational energy that dominates the kinematic energy. The observed increasing filament ridge intensities from outer to inner areas can be explained by the accretion flows accumulating nearby gas while at the same time continuously moving toward the center. However, we do not detect increasing velocity gradients along the filaments as they approach the center. This is possibly because we do not have sufficient resolution to resolve the velocity structures within the filaments. Liu et al. (2012a) have detected a velocity gradient of 0.96 km/s/pc along the filaments at ~ 0.1 pc scale within the inner 0.3 pc area of this system using SMA NH_3 (1,1) and (3,3) line data, which is higher than the velocity gradient of ~ 0.5 km/s/pc that we find in the hub center. This might support our speculation that the gas within the filaments is gravitationally accelerated near the center.

In the above emerging scenario, magnetic fields are expected to be dragged by the collapsing gas as simulated in Gómez et al. (2018), a model identical to Gómez &

Vázquez-Semadeni (2014) but with magnetic fields included. As a result, the magnetic fields are perpendicular to filaments in diffuse areas because the fields are dragged by the gas accreted onto the filaments. As density increases, the magnetic field lines become parallel to filaments because the fields are stretched by the longitudinal flow along the filaments. Our observed alignment between magnetic fields and filaments in dense areas supports this prediction. Our finding for the diffuse areas is clearly revealing a distribution different from the one for dense areas, being more random but also hinting a broader peak towards larger misalignments, i.e., field orientations perpendicular to filaments.

6. CONCLUSIONS

This paper presents the 850 μm JCMT SCUBA-2/POL-2 observations toward the G33.92+0.11 hub-filament system. Our observations reveal an organized but complex magnetic field morphology. From the analysis of these data, we find the following results.

- Filamentary structures are identified in G33.92+0.11 using the *DisPerSE* algorithm. The identified filaments appear as an overall converging network where most of the filaments either directly connect to the central hub or merge with other filaments connecting to the central hub. The filament converging points are generally located at local intensity peaks.
- The direction of local gravity, estimated from the 850 μm continuum data, mostly points toward the central hub and is prevalently aligned with the filament orientations. This provides some evidence that the filaments in this system are controlled by gravity. These filaments have widths varying from ~ 0.5 to ~ 0.8 pc as a function of the ridge intensity. This is different from the constant filament width seen in *Herschel* surveys.
- We further analyze the relative orientations between filaments, local gravity, magnetic field, and local LOS velocity gradients estimated from IRAM-30m C^{18}O (2-1) line data. The randomness of the distributions of these relative orientations is examined using KS-tests with a 95% confidence interval. The resulting statistics indicate that local gravity is aligned with filaments and the magnetic field in high-density regions. In low-density regions, the filaments are still aligned with local gravity, but shifting to becoming more perpendicular or random to the magnetic field and velocity gradients.

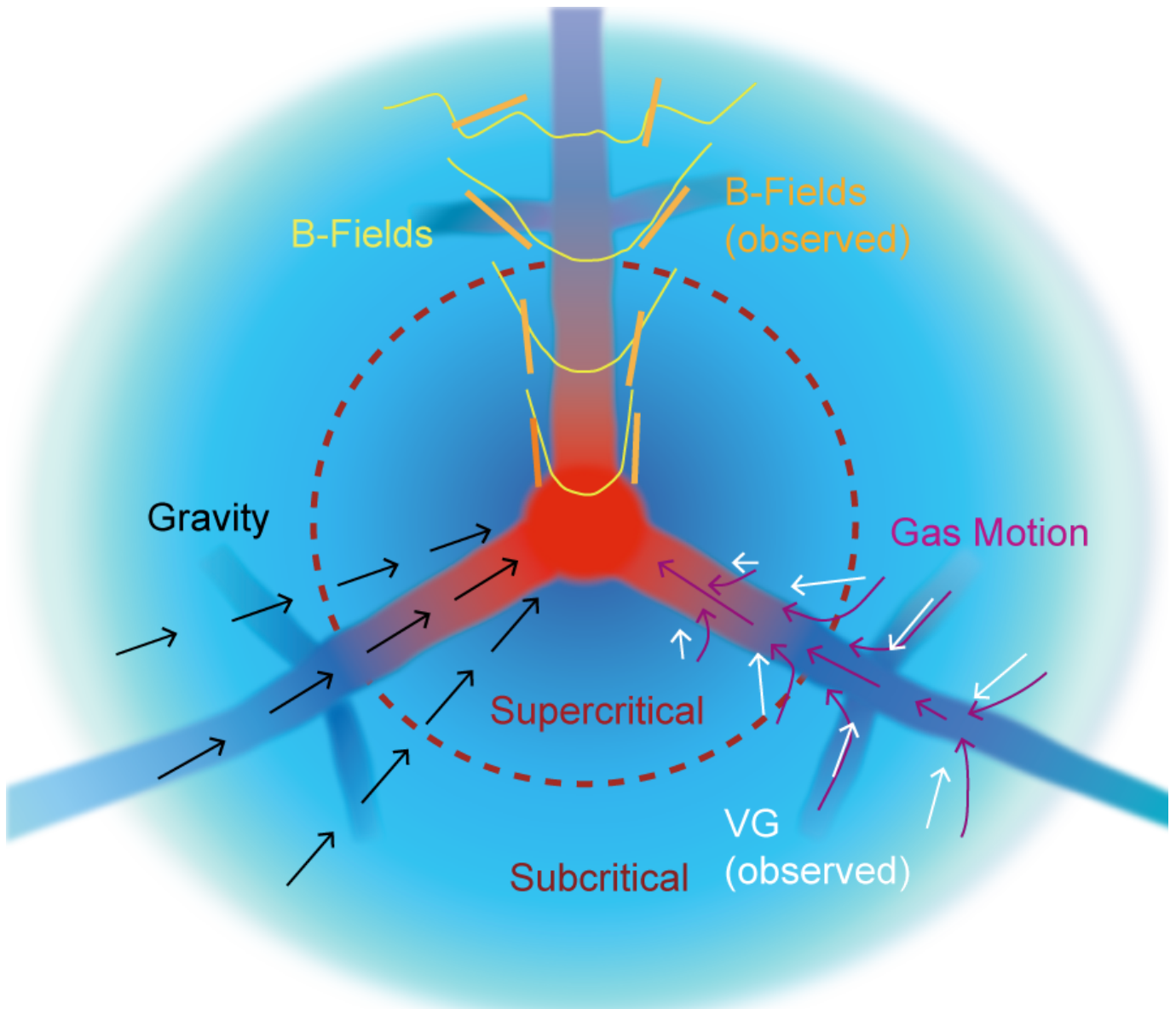


Figure 16. Cartoon illustrating observed features. The black arrows represent the directions of local gravity. The yellow curve shows a model-compatible magnetic field morphology (section 5.4) with the orange segments displaying the observed field segments with a spatial resolution (~ 0.5 pc) comparable to the filament widths (0.5–1 pc). The magenta arrows illustrate the directions of gas motion with the white arrows depicting the observed velocity gradients at the resolved 0.5-pc scale. The background color displays local density. In the diffuse outer areas, the ambient gas is accumulated onto the major filaments directly or via short streams, while the major filaments flow toward the central hub due to global gravity. Magnetic fields might be initially perpendicular to the major filaments, guiding the gas accumulation, but are then also dragged by the gas flows along the main filament. In the dense inner areas, the density of the major filaments grows through gathering mass from the surroundings. The increased ram pressure of the accretion flows can further stretch the magnetic field on the way to the center. This results in a magnetic field parallel to both the major filaments and local gravity. The magnitude of the velocity gradient decreases towards the center while the velocity dispersion increases. An outer subcritical and inner supercritical zone is indicated.

- Globally, the relative importance of gravitational, magnetic, and kinematic energy in G33.92+0.11 is estimated from a Virial equation. The analysis suggests that the gravitational energy dominates the system, while the kinematic is slightly larger than the magnetic energy by a factor of $\sim 1-2$. Hence, the system is likely collapsing, and the identified filaments are likely infalling accretion flows.
- Combining all findings from global properties and local correlations, we interpret G33.92+0.11 as a multi-scale gravitationally collapsing cloud with relatively weak turbulence and magnetic field. The ambient gas in the diffuse environment is accreted onto the filaments, while the filaments drag the magnetic field lines and flow toward the gravitational center. The observed local velocity gradients mainly trace the gas accumulation from the surrounding to the filaments, especially in low-density areas, and are thus perpendicular to the filaments. The observed magnetic field is stretched by the accretion flows, especially in high-density areas, and is therefore aligned with filaments and gravity.

The James Clerk Maxwell Telescope is operated by the East Asian Observatory on behalf of The National Astronomical Observatory of Japan; Academia Sinica

Institute of Astronomy and Astrophysics in Taiwan; the Korea Astronomy and Space Science Institute; the Operation, Maintenance and Upgrading Fund for Astronomical Telescopes and Facility Instruments, budgeted from the Ministry of Finance (MOF) of China and administrated by the Chinese Academy of Sciences (CAS), as well as the National Key R&D Program of China (No. 2017YFA0402700). Additional funding support is provided by the Science and Technology Facilities Council of the United Kingdom and participating universities in the United Kingdom and Canada. Additional funds for the construction of SCUBA-2 and POL-2 were provided by the Canada Foundation for Innovation. The Starlink software (Currie et al. 2014) is currently supported by the East Asian Observatory. The authors wish to recognize and acknowledge the very significant cultural role and reverence that the summit of Maunakea has always had within the indigenous Hawaiian community. We are most fortunate to have the opportunity to conduct observations from this mountain. J.W.W and P. M. K. acknowledge support from the Ministry of Science and Technology (MOST) grants MOST 108-2112-M-001-012 and MOST 109-2112-M-001-022, and from an Academia Sinica Career Development Award. S.P.L. is thankful to the support from the Ministry of Science and Technology of Taiwan through the grant MOST 106-2119-M-007-021-MY3. R.G.M. acknowledges support from UNAM-PAPIIT project IN104319.

APPENDIX

A. POLARIZATION PROPERTIES

Figure 17 shows the observed polarization map overlaid on the 850 μm total intensity images. Assuming that dust grains are aligned with the magnetic field is a fundamental assumption that allows us to use polarization data to trace magnetic fields. The relation between the total intensity (I) and the polarization fraction (P) is commonly used to examine this assumption. If the dust grains are not aligned with the magnetic field in a dense cloud, the observed polarized intensity (PI) would be independent of the cloud's column density, and thus $PI \propto I^0$ or $P = PI/I \propto I^{-1}$. In contrast, if magnetic-field-aligned dust grains are present in a dense cloud, we expect an increase of PI with the cloud's column density, and thus $PI \propto I^\alpha$ or $P \propto I^{-\alpha}$, where α is smaller than 1.

The observed I-P relation for G33.92+0.11 is displayed in Figure 18. We follow the Bayesian analysis in Wang et al. (2019) to determine the power-law index α of this relation: The model we use is a power-law

$$P = \beta I^{-\alpha}, \quad (\text{A1})$$

with a probability distribution function (PDF) of P described by the Rice distribution

$$F(P|P_0) = \frac{P}{\sigma_P^2} \exp\left[-\frac{P^2 + P_0^2}{2\sigma_P^2}\right] I_0\left(\frac{PP_0}{\sigma_P^2}\right), \quad (\text{A2})$$

where P is the observed polarization fraction, P_0 is the real polarization fraction, σ_P is the uncertainty in the polarization fraction, and I_0 is the zeroth-order modified Bessel function. We further assume that the uncertainty in the polarization fraction is given by

$$\sigma_P = \sigma/I, \quad (\text{A3})$$

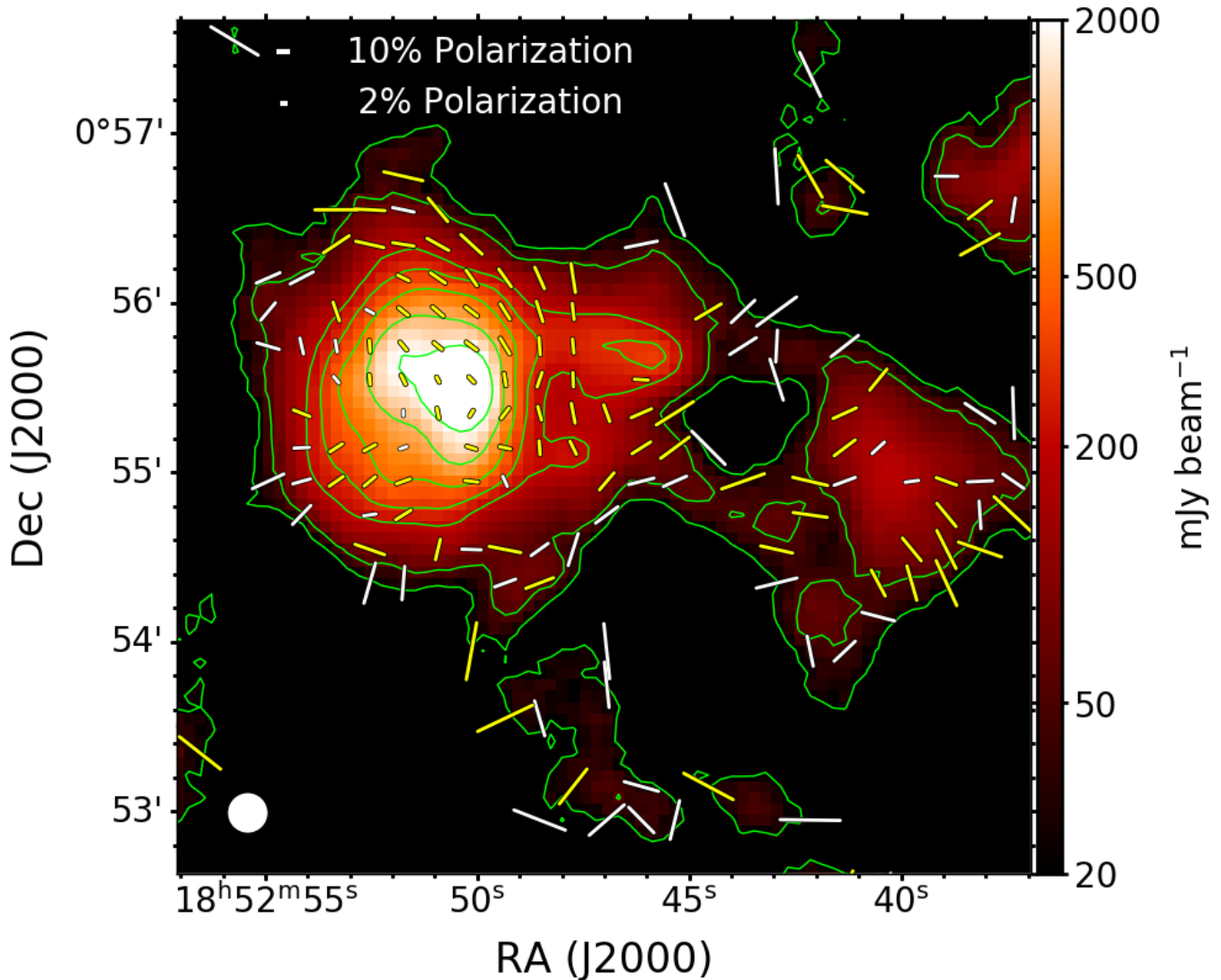


Figure 17. Polarization (segments) sampled on a $12''$ grid overlaid on $850 \mu\text{m}$ dust continuum (color and contours), sampled on a $4''$ grid, of the G33.92+0.11 region. The segments are selected with the criteria $I/\sigma_I > 10$ and $P/\sigma_P > 2$. The yellow and white segments display the larger than 3σ and $2-3\sigma$ polarization detections. The lengths of the segments are proportional to the square root of the polarization fraction. The white segments in the upper left corner are examples of 2% and 10% polarization fractions. The green contours show the total intensity at 20, 50, 200, 300, 500, 1000, and 2000 mJy beam^{-1} . The white circle in the bottom left corner is the JCMT beam size of $14''$. The rms noise of the Stokes I is $\sim 1-5 \text{ mJy beam}^{-1}$ depends on pixel intensities, within the central $3'$ area.

where σ is the uncertainty of Stokes Q and U. We, nevertheless, treat σ as an unknown parameter here because the dispersion in the observed P is not only coming from the observational uncertainty but also from the intrinsic dispersion within G33.92+0.11.

Since the distribution of the Ricean noise is well accounted for in this model, we can directly use the non-selected, non-debiased polarization data to compare with the model. Hence, in Figure 18, we use all the raw polarization data for the Bayesian analysis, except for the edge pixels or the possible artificial patterns selected by the criteria $\sigma_I > 5 \text{ mJy beam}^{-1}$ and $I/\sigma_I > 3$. The computed posterior distributions of the Bayesian analysis are shown in Figure 19. α is expected to be $0.42_{-0.07}^{+0.09}$ which is significantly smaller than 1. This suggests that aligned dust grains are present within G33.92+0.11, and hence the observed polarization patterns likely trace the magnetic field morphology.

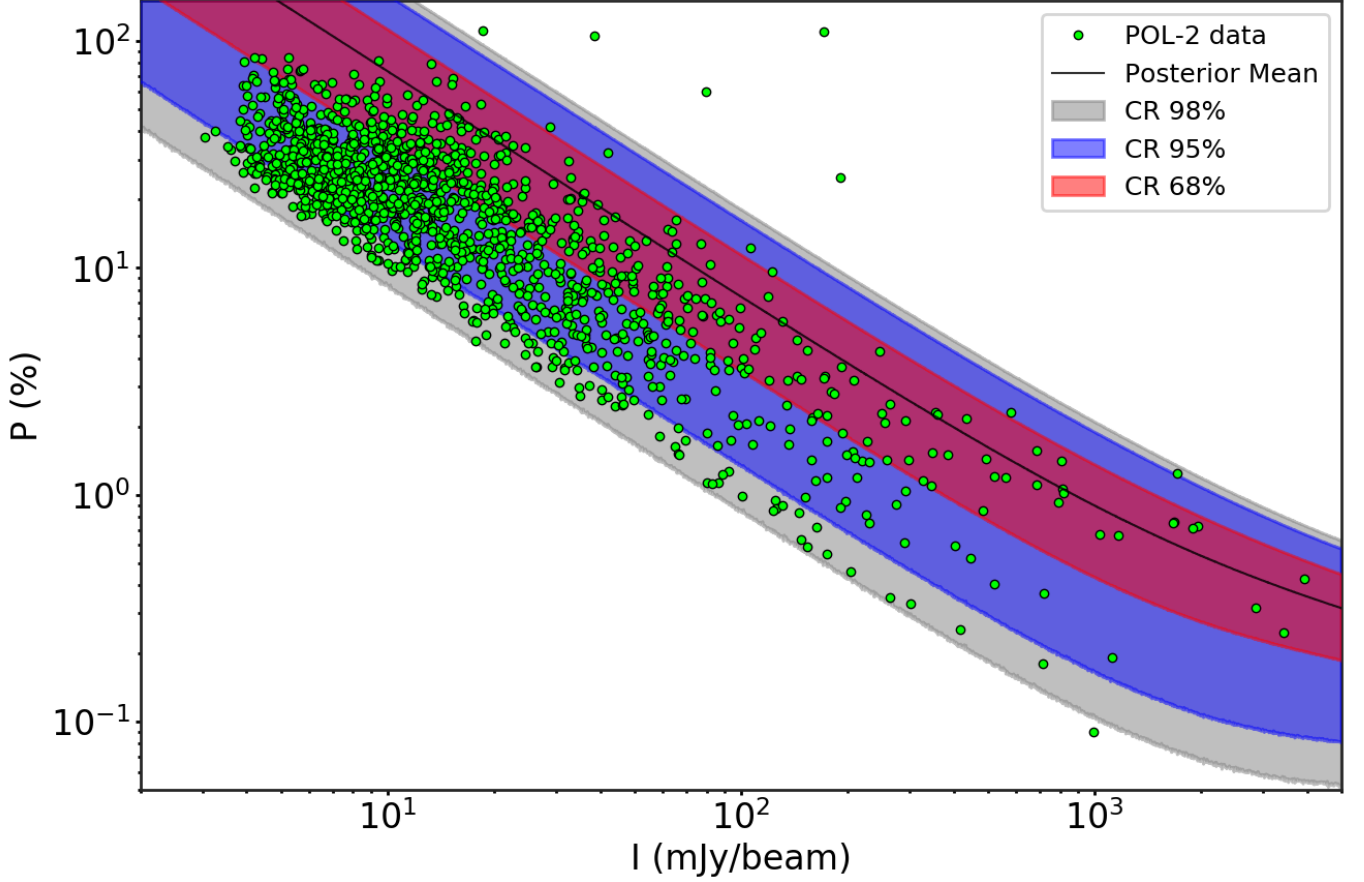


Figure 18. $850\ \mu\text{m}$ total intensity I vs polarization fraction P . The green points are the non-debiased, $I/\sigma_I > 3$, and $\sigma_I < 5\ \text{mJy beam}^{-1}$ POL-2 polarization measurements. The colored regions are the predicted I-P distributions based on the Bayesian analysis within the 68%, 95%, and 98% confidence region (CR). The black line indicates the posterior mean. Most of the data points are within the 98% confidence region of our prediction.

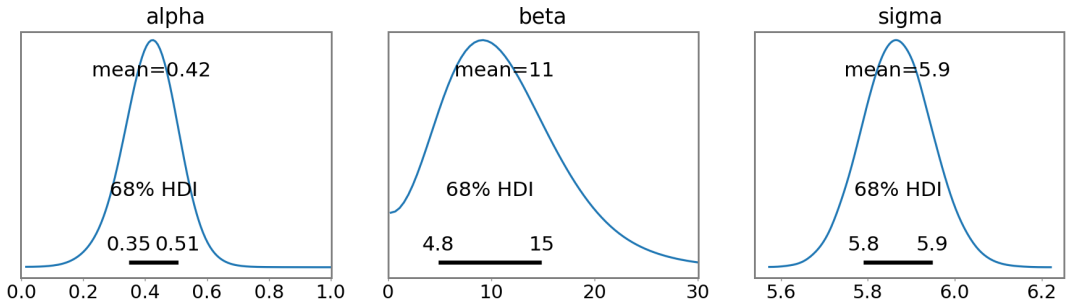


Figure 19. Posterior distributions from Bayesian analysis for I-P relation. The black lines delineate the 68% (1σ) highest density interval (HDI). α is expected to be significantly less than 1 with $0.42^{+0.09}_{-0.07}$, suggesting that aligned dust grains are present within G33.92+0.11.

B. PAIRWISE DIFFERENTIAL ORIENTATIONS BETWEEN FILAMENTS, MAGNETIC FIELD, LOCAL GRAVITY, AND LOCAL VELOCITY GRADIENTS

Figure 20 presents all combinations of pairwise differential orientations between filaments, magnetic field, local gravity, and local velocity gradients, spatially overlaid on the $850\ \mu\text{m}$ dust continuum map. The first column is identical to Figure 11. The VG-B and VG-G plots might display tendencies of the local velocity gradient being

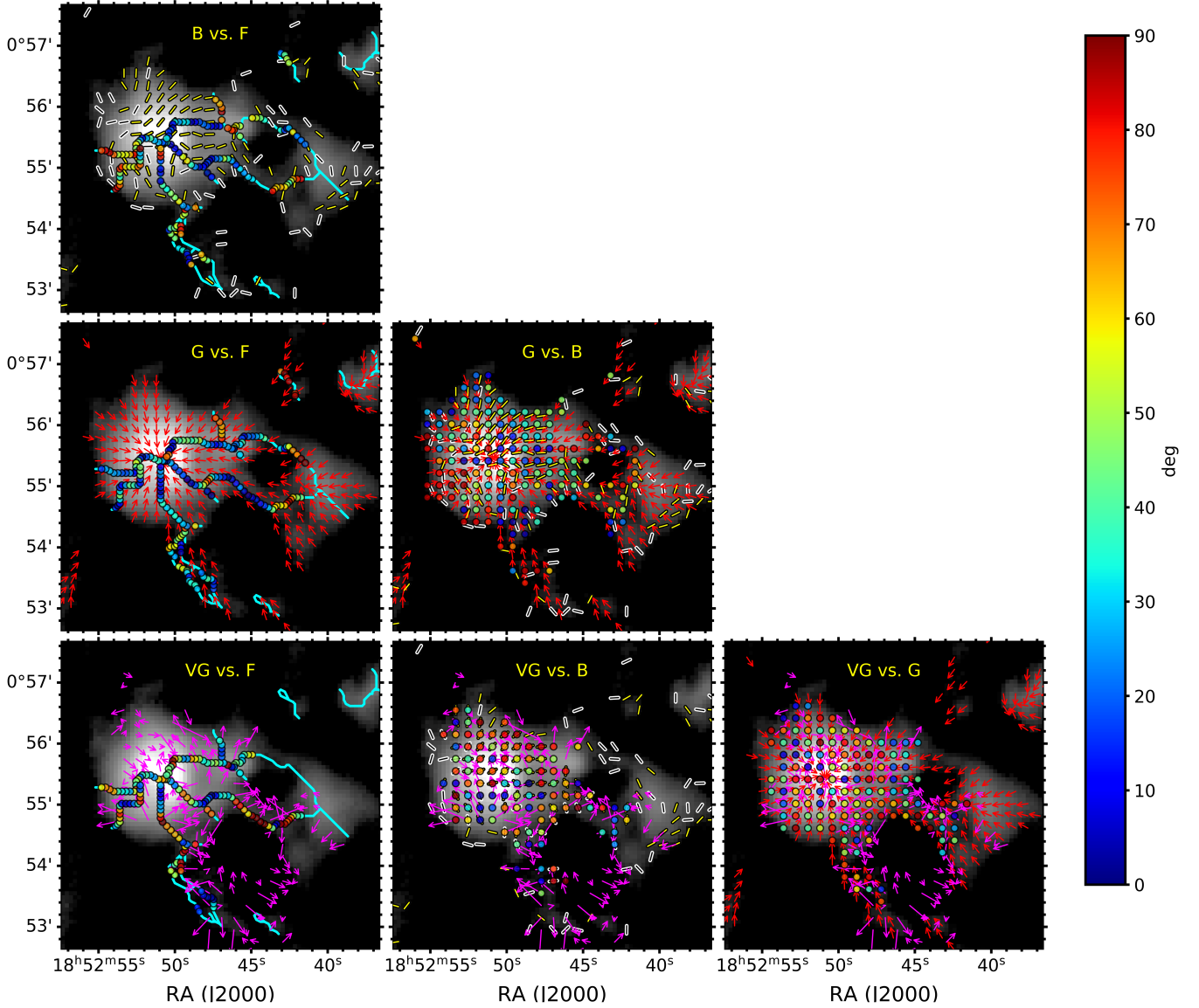


Figure 20. Pairwise differential orientation maps between filaments, magnetic field, local gravity, and local velocity gradients, overlaid on $850\ \mu\text{m}$ dust continuum. The cyan lines are the filaments identified in Figure 3. The yellow and black segments represent the magnetic field orientations as shown in Figure 1, the red arrows are the projected local gravity, and the magenta arrows show the local velocity gradients. Filled color-coded circles (color wedge) are the pairwise differential orientations ΔPA .

perpendicular to local gravity and magnetic field away from the hub center, except for some regions located in between filaments. However, our spatial resolution is insufficient to probe this possible change from on-filament to off-filament regions in more detail. The G–B plot generally shows that the magnetic field is aligned with local gravity near the hub center. Only a few exceptions are found at the northern side of the C1 converging point. These exceptions are at the center of two filaments, where we find that the magnetic field orientations change significantly (from $PA \sim 135^\circ$ to 90° at C1, and from $PA \sim 10^\circ$ to 90° at C3). Hence, we speculate that the observed magnetic field structure in these areas is possibly the result of the merging of two nearby filaments, and thus the alignment between magnetic field and local gravity is perturbed.

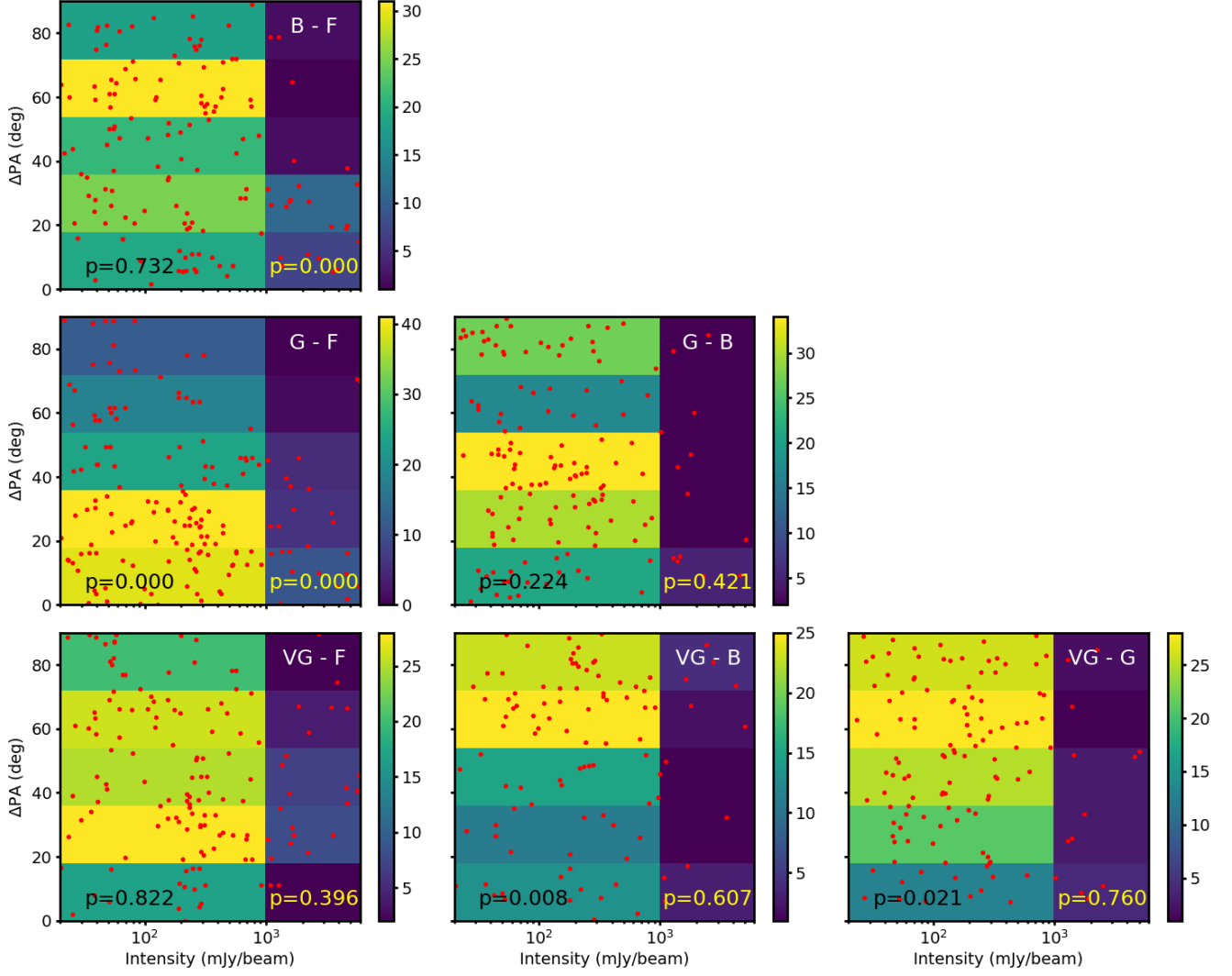


Figure 21. Pairwise differential orientations between filaments, magnetic field, local gravity, and local velocity gradients versus intensity. The red points represent the ΔPA of the pairwise parameters (indicated in the upper right corner in each panel) as a function of the local intensity at spatially matched pixels/segments/vectors. The background color indicates the density of red data points given with the color wedge. The data set in each panel is separated into a low- and high-intensity group, below and above $I_{850} = 1000 \text{ mJy beam}^{-1}$. KS tests are applied and p-values are given for each group separately. The comparison between the ΔPA distributions in the low- and high-intensity areas reveals a tightening alignment between filaments, gravity, and magnetic fields with growing intensity, while the local velocity structures become more disordered.

C. DEPENDENCE OF FILAMENTS, MAGNETIC FIELD, LOCAL GRAVITY, AND LOCAL VELOCITY GRADIENTS ON INTENSITY

Figure 21 shows the distribution of ΔPA and total intensity for all the associated filaments, magnetic field, local gravity, and local velocity gradient pairs. The data set in each panel is separated into a low- and high-intensity group, below and above $I_{850} = 1000 \text{ mJy beam}^{-1}$. The B-F, VG-B, and VG-G pairs show different ΔPA distributions between low- and high-density areas, which are also shown in Figure 12. We note that the high-density groups mostly contain only 10–30 data points, and thus the high p-value can be due to the small sample sizes.

D. FILAMENT IDENTIFICATION THRESHOLD

In order to investigate how a filament identification threshold possibly affects our results in Section 4.4 (Figure 11, Figure 9, and Figure 21), we have repeated our analysis with a lower threshold of 20 mJy beam^{-1} . The KS-tests still

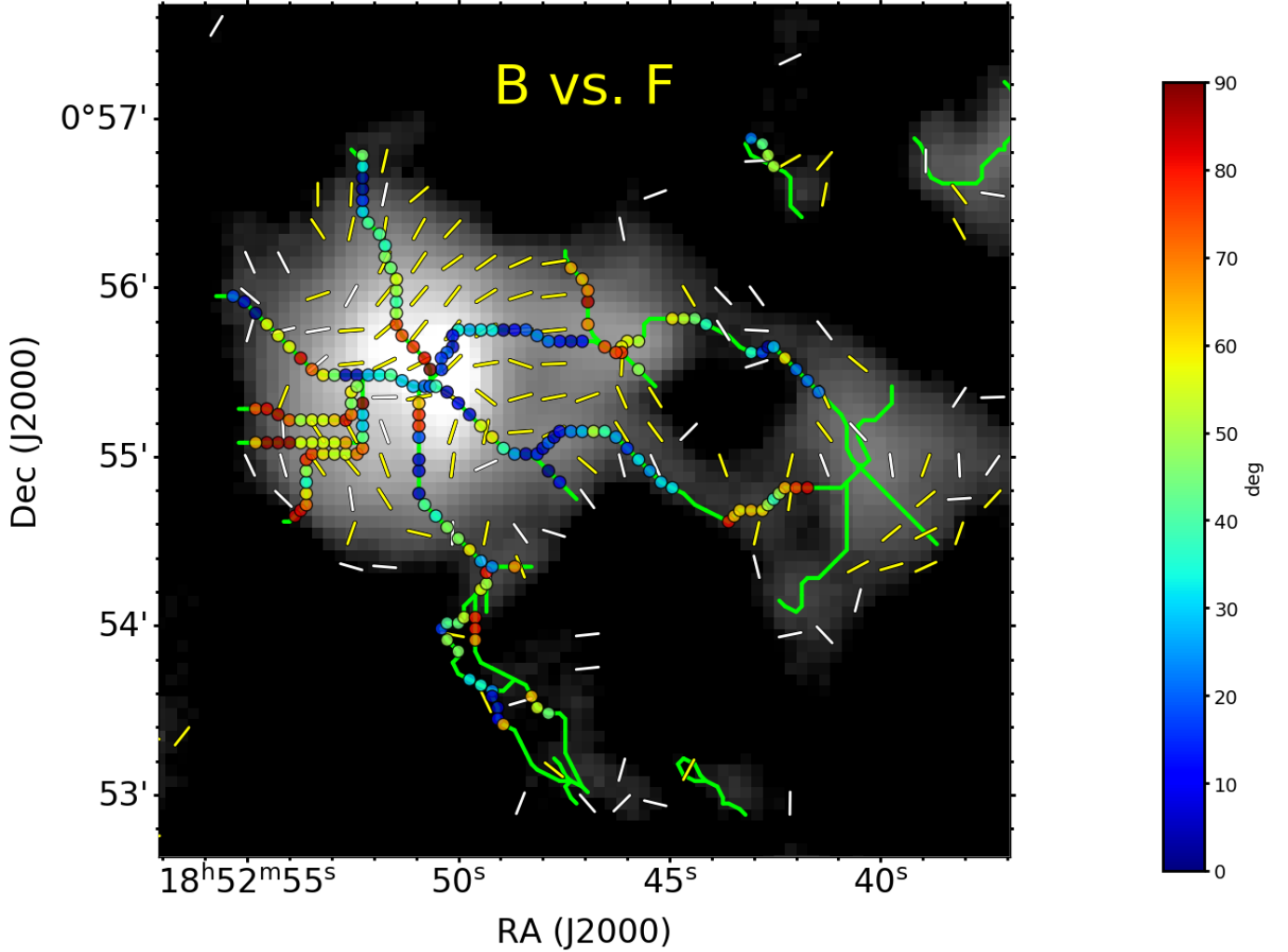


Figure 22. Differential orientation map for filaments (F) vs magnetic fields (B), where the filaments are identified with a lower threshold of 20 mJy beam^{-1} . The yellow and white segments are the magnetic field orientations as shown in Figure 1. The color-coded circles are the differential orientations B vs F.

reveal correlations identical to the results in Section 4.4 for a higher threshold. The only exception is the p-value for the B–F relation in dense regions. This value increases from < 0.001 to 0.055 , as a result of a histogram originally peaking around small values (top panel in Figure 12) now shifting to a more bimodal ΔPA distribution around 0° and 90° (Figure 23). These more perpendicular B–F pairs can be traced back to a newly located weaker filament extending from the central hub to the north (Figure 22). Around this location, the magnetic field seems to be more aligned with the nearby filament extending toward the west, and not with the new filament toward the north. Since these two filaments merge into the central hub and are separated by only $\sim 0.5\text{--}1 \text{ pc}$ (less than two times the filament width of $1\text{--}1.5 \text{ pc}$), it is likely that the observed polarization here mainly traces the magnetic field around the denser filament to the west. These leads to the few perpendicular B–F pairs. However, it has to be acknowledged that the limited resolution does not really allow us to fully separate these two filaments near the center. We, therefore, conclude that our results from Section 4.4 remain robust and largely unaffected if the detection threshold for filaments is lowered to 20 mJy beam^{-1} .

Facilities: JCMT,IRAM:30m

Software: Aplan (Robitaille & Bressert 2012; Robitaille 2019), Astropy (Astropy Collaboration et al. 2013, 2018), DisPerSE (Sousbie 2011), FilChap (Suri et al. 2019), GILDAS/CLASS (Pety 2005; Gildas Team 2013), NumPy (Oliphant

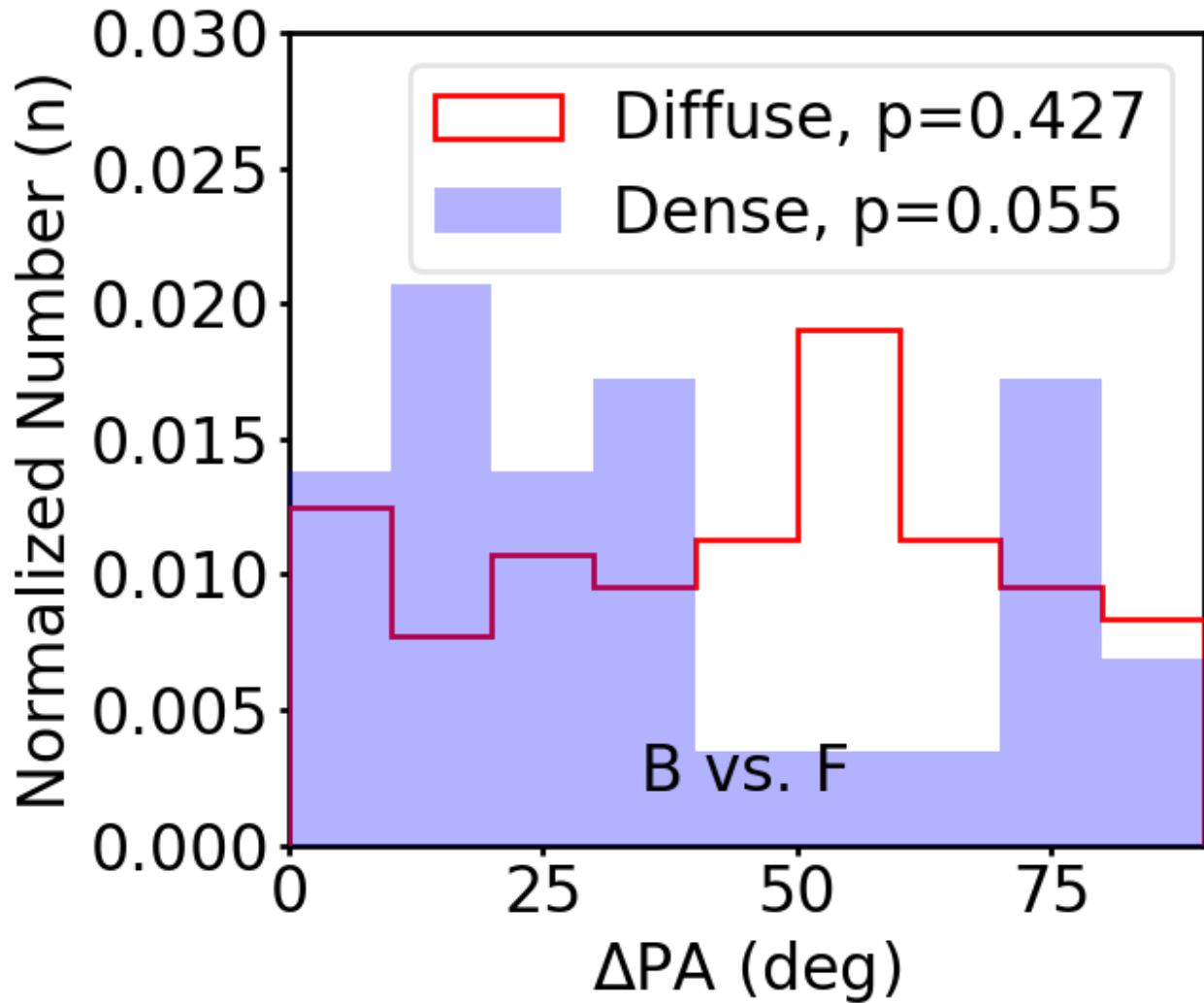


Figure 23. Normalized histograms of differential orientations between filaments, identified with a lower threshold of 20 mJy beam^{-1} , and magnetic field, separated by local intensity. The blue and red histograms represent the data selected in the dense ($I_{850} > 1000 \text{ mJy beam}^{-1}$) and the diffuse ($I_{850} < 1000 \text{ mJy beam}^{-1}$) areas. The KS-test results against a random distribution are listed for these two groups.

2006–), SciPy (Virtanen et al. 2019), PySpecKit (Ginsburg & Mirocha 2011), Smurf (Berry et al. 2005; Chapin et al. 2013), Starlink (Currie et al. 2014)

REFERENCES

- André, P., Di Francesco, J., Ward-Thompson, D., et al. 2014, in *Protostars and Planets VI*, ed. H. Beuther, R. S. Klessen, C. P. Dullemond, & T. Henning, 27
- André, P., Men'shchikov, A., Bontemps, S., et al. 2010, *A&A*, 518, L102, doi: [10.1051/0004-6361/201014666](https://doi.org/10.1051/0004-6361/201014666)
- Arzoumanian, D., André, P., Peretto, N., & Könyves, V. 2013, *A&A*, 553, A119, doi: [10.1051/0004-6361/201220822](https://doi.org/10.1051/0004-6361/201220822)
- Arzoumanian, D., Furuya, R. S., Hasegawa, T., & the BISTRO consortium. 2020, submitted to *ApJ*
- Arzoumanian, D., André, P., Didelon, P., et al. 2011, *A&A*, 529, L6, doi: [10.1051/0004-6361/201116596](https://doi.org/10.1051/0004-6361/201116596)
- Arzoumanian, D., André, P., Könyves, V., et al. 2019, *A&A*, 621, A42, doi: [10.1051/0004-6361/201832725](https://doi.org/10.1051/0004-6361/201832725)
- Astropy Collaboration, Robitaille, T. P., Tollerud, E. J., et al. 2013, *A&A*, 558, A33, doi: [10.1051/0004-6361/201322068](https://doi.org/10.1051/0004-6361/201322068)
- Astropy Collaboration, Price-Whelan, A. M., Sipőcz, B. M., et al. 2018, *AJ*, 156, 123, doi: [10.3847/1538-3881/aabc4f](https://doi.org/10.3847/1538-3881/aabc4f)
- Berry, D. S., Gledhill, T. M., Greaves, J. S., & Jenness, T. 2005, in *Astronomical Society of the Pacific Conference Series*, Vol. 343, *Astronomical Polarimetry: Current Status and Future Directions*, ed. A. Adamson, C. Aspin, C. Davis, & T. Fujiyoshi, 71
- Chandrasekhar, S., & Fermi, E. 1953, *ApJ*, 118, 113, doi: [10.1086/145731](https://doi.org/10.1086/145731)
- Chapin, E. L., Berry, D. S., Gibb, A. G., et al. 2013, *MNRAS*, 430, 2545, doi: [10.1093/mnras/stt052](https://doi.org/10.1093/mnras/stt052)
- Chen, C.-Y., Mundy, L. G., Ostriker, E. C., Storm, S., & Dhabal, A. 2020a, *MNRAS*, 494, 3675, doi: [10.1093/mnras/staa960](https://doi.org/10.1093/mnras/staa960)
- Chen, C.-Y., & Ostriker, E. C. 2014, *ApJ*, 785, 69, doi: [10.1088/0004-637X/785/1/69](https://doi.org/10.1088/0004-637X/785/1/69)
- . 2015, *ApJ*, 810, 126, doi: [10.1088/0004-637X/810/2/126](https://doi.org/10.1088/0004-637X/810/2/126)
- Chen, M. C.-Y., Francesco, J. D., Rosolowsky, E., et al. 2020b, *ApJ*, 891, 84, doi: [10.3847/1538-4357/ab7378](https://doi.org/10.3847/1538-4357/ab7378)
- Cox, N. L. J., Arzoumanian, D., André, P., et al. 2016, *A&A*, 590, A110, doi: [10.1051/0004-6361/201527068](https://doi.org/10.1051/0004-6361/201527068)
- Crutcher, R. M., Nutter, D. J., Ward-Thompson, D., & Kirk, J. M. 2004, *ApJ*, 600, 279, doi: [10.1086/379705](https://doi.org/10.1086/379705)
- Cudlip, W., Furniss, I., King, K. J., & Jennings, R. E. 1982, *MNRAS*, 200, 1169, doi: [10.1093/mnras/200.4.1169](https://doi.org/10.1093/mnras/200.4.1169)
- Currie, M. J., Berry, D. S., Jenness, T., et al. 2014, in *Astronomical Society of the Pacific Conference Series*, Vol. 485, *Astronomical Data Analysis Software and Systems XXIII*, ed. N. Manset & P. Forshay, 391
- Davis, L. 1951, *Physical Review*, 81, 890, doi: [10.1103/PhysRev.81.890.2](https://doi.org/10.1103/PhysRev.81.890.2)
- Dempsey, J. T., Friberg, P., Jenness, T., et al. 2013, *MNRAS*, 430, 2534, doi: [10.1093/mnras/stt090](https://doi.org/10.1093/mnras/stt090)
- Dobashi, K., Matsumoto, T., Shimoikura, T., et al. 2014, *ApJ*, 797, 58, doi: [10.1088/0004-637X/797/1/58](https://doi.org/10.1088/0004-637X/797/1/58)
- Doi, Y., Hasegawa, T., Furuya, R. S., et al. 2020, arXiv e-prints, arXiv:2007.00176, <https://arxiv.org/abs/2007.00176>
- Federrath, C. 2016, *MNRAS*, 457, 375, doi: [10.1093/mnras/stv2880](https://doi.org/10.1093/mnras/stv2880)
- Fernández-López, M., Arce, H. G., Looney, L., et al. 2014, *ApJL*, 790, L19, doi: [10.1088/2041-8205/790/2/L19](https://doi.org/10.1088/2041-8205/790/2/L19)
- Fiege, J. D., & Pudritz, R. E. 2000, *MNRAS*, 311, 105, doi: [10.1046/j.1365-8711.2000.03067.x](https://doi.org/10.1046/j.1365-8711.2000.03067.x)
- Fischera, J., & Martin, P. G. 2012, *A&A*, 542, A77, doi: [10.1051/0004-6361/201218961](https://doi.org/10.1051/0004-6361/201218961)
- Fish, V. L., Reid, M. J., Wilner, D. J., & Churchwell, E. 2003, *ApJ*, 587, 701, doi: [10.1086/368284](https://doi.org/10.1086/368284)
- Frau, P., Girart, J. M., Alves, F. O., et al. 2015, *A&A*, 574, L6, doi: [10.1051/0004-6361/201425234](https://doi.org/10.1051/0004-6361/201425234)
- Friberg, P., Bastien, P., Berry, D., et al. 2016, in *Society of Photo-Optical Instrumentation Engineers (SPIE) Conference Series*, Vol. 9914, *Millimeter, Submillimeter, and Far-Infrared Detectors and Instrumentation for Astronomy VIII*, 991403
- Friesen, R. K., Medeiros, L., Schnee, S., et al. 2013, *MNRAS*, 436, 1513, doi: [10.1093/mnras/stt1671](https://doi.org/10.1093/mnras/stt1671)
- Galván-Madrid, R., Liu, H. B., Zhang, Z. Y., et al. 2013, *ApJ*, 779, 121, doi: [10.1088/0004-637X/779/2/121](https://doi.org/10.1088/0004-637X/779/2/121)
- Gildas Team. 2013, *GILDAS: Grenoble Image and Line Data Analysis Software*. <http://ascl.net/1305.010>
- Ginsburg, A., & Mirocha, J. 2011, *PySpecKit: Python Spectroscopic Toolkit*. <http://ascl.net/1109.001>
- Goldsmith, P. F., Heyer, M., Narayanan, G., et al. 2008, *ApJ*, 680, 428, doi: [10.1086/587166](https://doi.org/10.1086/587166)
- Gómez, G. C., & Vázquez-Semadeni, E. 2014, *ApJ*, 791, 124, doi: [10.1088/0004-637X/791/2/124](https://doi.org/10.1088/0004-637X/791/2/124)
- Gómez, G. C., Vázquez-Semadeni, E., & Zamora-Avilés, M. 2018, *MNRAS*, 480, 2939, doi: [10.1093/mnras/sty2018](https://doi.org/10.1093/mnras/sty2018)
- Gong, H., & Ostriker, E. C. 2011, *ApJ*, 729, 120, doi: [10.1088/0004-637X/729/2/120](https://doi.org/10.1088/0004-637X/729/2/120)
- Gutermuth, R. A., Megeath, S. T., Myers, P. C., et al. 2009, *ApJS*, 184, 18, doi: [10.1088/0067-0049/184/1/18](https://doi.org/10.1088/0067-0049/184/1/18)
- Hacar, A., Tafalla, M., Forbrich, J., et al. 2018, *A&A*, 610, A77, doi: [10.1051/0004-6361/201731894](https://doi.org/10.1051/0004-6361/201731894)
- Heitsch, F. 2013a, *ApJ*, 769, 115, doi: [10.1088/0004-637X/769/2/115](https://doi.org/10.1088/0004-637X/769/2/115)
- . 2013b, *ApJ*, 776, 62, doi: [10.1088/0004-637X/776/1/62](https://doi.org/10.1088/0004-637X/776/1/62)
- Heyer, M., Krawczyk, C., Duval, J., & Jackson, J. M. 2009, *ApJ*, 699, 1092, doi: [10.1088/0004-637X/699/2/1092](https://doi.org/10.1088/0004-637X/699/2/1092)

- Hildebrand, R. H. 1983, QJRAS, 24, 267
- . 1988, QJRAS, 29, 327
- Houde, M., Vaillancourt, J. E., Hildebrand, R. H., Chitsazzadeh, S., & Kirby, L. 2009, ApJ, 706, 1504, doi: [10.1088/0004-637X/706/2/1504](https://doi.org/10.1088/0004-637X/706/2/1504)
- Kauffmann, J., Pillai, T., & Goldsmith, P. F. 2013, ApJ, 779, 185, doi: [10.1088/0004-637X/779/2/185](https://doi.org/10.1088/0004-637X/779/2/185)
- Kirk, H., Myers, P. C., Bourke, T. L., et al. 2013, ApJ, 766, 115, doi: [10.1088/0004-637X/766/2/115](https://doi.org/10.1088/0004-637X/766/2/115)
- Koch, P. M., Tang, Y.-W., & Ho, P. T. P. 2012a, ApJ, 747, 79, doi: [10.1088/0004-637X/747/1/79](https://doi.org/10.1088/0004-637X/747/1/79)
- . 2012b, ApJ, 747, 80, doi: [10.1088/0004-637X/747/1/80](https://doi.org/10.1088/0004-637X/747/1/80)
- . 2013, ApJ, 775, 77, doi: [10.1088/0004-637X/775/1/77](https://doi.org/10.1088/0004-637X/775/1/77)
- Koch, P. M., Tang, Y.-W., Ho, P. T. P., et al. 2014, ApJ, 797, 99, doi: [10.1088/0004-637X/797/2/99](https://doi.org/10.1088/0004-637X/797/2/99)
- Kwon, J., Doi, Y., Tamura, M., et al. 2018, ApJ, 859, 4, doi: [10.3847/1538-4357/aabd82](https://doi.org/10.3847/1538-4357/aabd82)
- Lada, C. J., & Lada, E. A. 2003, ARA&A, 41, 57, doi: [10.1146/annurev.astro.41.011802.094844](https://doi.org/10.1146/annurev.astro.41.011802.094844)
- Larson, R. B. 1981, MNRAS, 194, 809, doi: [10.1093/mnras/194.4.809](https://doi.org/10.1093/mnras/194.4.809)
- Li, H. B., Goodman, A., Sridharan, T. K., et al. 2014, in Protostars and Planets VI, ed. H. Beuther, R. S. Klessen, C. P. Dullemond, & T. Henning, 101
- Li, H.-b., & Houde, M. 2008, ApJ, 677, 1151, doi: [10.1086/529581](https://doi.org/10.1086/529581)
- Li, P. S., & Klein, R. I. 2019, MNRAS, 485, 4509, doi: [10.1093/mnras/stz653](https://doi.org/10.1093/mnras/stz653)
- Liu, H. B., Galván-Madrid, R., Jiménez-Serra, I., et al. 2015, ApJ, 804, 37, doi: [10.1088/0004-637X/804/1/37](https://doi.org/10.1088/0004-637X/804/1/37)
- Liu, H. B., Jiménez-Serra, I., Ho, P. T. P., et al. 2012a, ApJ, 756, 10, doi: [10.1088/0004-637X/756/1/10](https://doi.org/10.1088/0004-637X/756/1/10)
- Liu, H. B., Quintana-Lacaci, G., Wang, K., et al. 2012b, ApJ, 745, 61, doi: [10.1088/0004-637X/745/1/61](https://doi.org/10.1088/0004-637X/745/1/61)
- Liu, H. B., Chen, H.-R. V., Román-Zúñiga, C. G., et al. 2019, ApJ, 871, 185, doi: [10.3847/1538-4357/aaf6b4](https://doi.org/10.3847/1538-4357/aaf6b4)
- McKee, C. F., & Ostriker, E. C. 2007, ARA&A, 45, 565, doi: [10.1146/annurev.astro.45.051806.110602](https://doi.org/10.1146/annurev.astro.45.051806.110602)
- McKee, C. F., & Tan, J. C. 2003, ApJ, 585, 850, doi: [10.1086/346149](https://doi.org/10.1086/346149)
- Mestel, L., & Spitzer, L., J. 1956, MNRAS, 116, 503, doi: [10.1093/mnras/116.5.503](https://doi.org/10.1093/mnras/116.5.503)
- Myers, P. C. 2009, ApJ, 700, 1609, doi: [10.1088/0004-637X/700/2/1609](https://doi.org/10.1088/0004-637X/700/2/1609)
- Nakamura, F., & Li, Z.-Y. 2008, ApJ, 687, 354, doi: [10.1086/591641](https://doi.org/10.1086/591641)
- Nakamura, F., Sugitani, K., Tanaka, T., et al. 2014, ApJL, 791, L23, doi: [10.1088/2041-8205/791/2/L23](https://doi.org/10.1088/2041-8205/791/2/L23)
- Nakano, T., & Nakamura, T. 1978, PASJ, 30, 671
- Nishimura, A., Tokuda, K., Kimura, K., et al. 2015, ApJS, 216, 18, doi: [10.1088/0067-0049/216/1/18](https://doi.org/10.1088/0067-0049/216/1/18)
- Oliphant, T. 2006–, NumPy: A guide to NumPy, USA: Trelgol Publishing. <http://www.numpy.org/>
- Ostriker, E. C., Stone, J. M., & Gammie, C. F. 2001, ApJ, 546, 980, doi: [10.1086/318290](https://doi.org/10.1086/318290)
- Padoan, P., Goodman, A., Draine, B. T., et al. 2001a, ApJ, 559, 1005, doi: [10.1086/322504](https://doi.org/10.1086/322504)
- Padoan, P., Juvela, M., Goodman, A. A., & Nordlund, Å. 2001b, ApJ, 553, 227, doi: [10.1086/320636](https://doi.org/10.1086/320636)
- Palmeirim, P., André, P., Kirk, J., et al. 2013, A&A, 550, A38, doi: [10.1051/0004-6361/201220500](https://doi.org/10.1051/0004-6361/201220500)
- Peretto, N., André, P., Könyves, V., et al. 2012, A&A, 541, A63, doi: [10.1051/0004-6361/201118663](https://doi.org/10.1051/0004-6361/201118663)
- Peretto, N., Fuller, G. A., André, P., et al. 2014, A&A, 561, A83, doi: [10.1051/0004-6361/201322172](https://doi.org/10.1051/0004-6361/201322172)
- Pety, J. 2005, in SF2A-2005: Semaine de l’Astrophysique Française, ed. F. Casoli, T. Contini, J. M. Hameury, & L. Pagani, 721
- Planck Collaboration, Ade, P. A. R., Aghanim, N., et al. 2016, A&A, 586, A138, doi: [10.1051/0004-6361/201525896](https://doi.org/10.1051/0004-6361/201525896)
- Robitaille, T. 2019, APLpy v2.0: The Astronomical Plotting Library in Python, doi: [10.5281/zenodo.2567476](https://doi.org/10.5281/zenodo.2567476), <https://doi.org/10.5281/zenodo.2567476>
- Robitaille, T., & Bressert, E. 2012, APLpy: Astronomical Plotting Library in Python, Astrophysics Source Code Library. <http://ascl.net/1208.017>
- Santos, F. P., Busquet, G., Franco, G. A. P., Girart, J. M., & Zhang, Q. 2016, ApJ, 832, 186, doi: [10.3847/0004-637X/832/2/186](https://doi.org/10.3847/0004-637X/832/2/186)
- Schneider, N., Csengeri, T., Hennemann, M., et al. 2012, A&A, 540, L11, doi: [10.1051/0004-6361/201118566](https://doi.org/10.1051/0004-6361/201118566)
- Shimajiri, Y., André, P., Palmeirim, P., et al. 2019, A&A, 623, A16, doi: [10.1051/0004-6361/201834399](https://doi.org/10.1051/0004-6361/201834399)
- Shu, F. H., Adams, F. C., & Lizano, S. 1987, ARA&A, 25, 23, doi: [10.1146/annurev.aa.25.090187.000323](https://doi.org/10.1146/annurev.aa.25.090187.000323)
- Sokolov, V., Wang, K., Pineda, J. E., et al. 2019, ApJ, 872, 30, doi: [10.3847/1538-4357/aafaff](https://doi.org/10.3847/1538-4357/aafaff)
- Sousbie, T. 2011, MNRAS, 414, 350, doi: [10.1111/j.1365-2966.2011.18394.x](https://doi.org/10.1111/j.1365-2966.2011.18394.x)
- Stone, J. M., Ostriker, E. C., & Gammie, C. F. 1998, ApJL, 508, L99, doi: [10.1086/311718](https://doi.org/10.1086/311718)
- Sugitani, K., Nakamura, F., Watanabe, M., et al. 2011, ApJ, 734, 63, doi: [10.1088/0004-637X/734/1/63](https://doi.org/10.1088/0004-637X/734/1/63)
- Suri, S., Sánchez-Monge, Á., Schilke, P., et al. 2019, A&A, 623, A142, doi: [10.1051/0004-6361/201834049](https://doi.org/10.1051/0004-6361/201834049)
- Tang, Y.-W., Koch, P. M., Peretto, N., et al. 2019, ApJ, 878, 10, doi: [10.3847/1538-4357/ab1484](https://doi.org/10.3847/1538-4357/ab1484)

- Traficante, A., Fuller, G. A., Duarte-Cabral, A., et al. 2020, MNRAS, 491, 4310, doi: [10.1093/mnras/stz3344](https://doi.org/10.1093/mnras/stz3344)
- Treviño-Morales, S. P., Fuente, A., Sánchez-Monge, Á., et al. 2019, A&A, 629, A81, doi: [10.1051/0004-6361/201935260](https://doi.org/10.1051/0004-6361/201935260)
- Van Loo, S., Keto, E., & Zhang, Q. 2014, ApJ, 789, 37, doi: [10.1088/0004-637X/789/1/37](https://doi.org/10.1088/0004-637X/789/1/37)
- Virtanen, P., Gommers, R., Oliphant, T. E., et al. 2019, arXiv e-prints, arXiv:1907.10121. <https://arxiv.org/abs/1907.10121>
- Wang, J.-W., Lai, S.-P., Clemens, D. P., et al. 2020, ApJ, 888, 13, doi: [10.3847/1538-4357/ab5c1c](https://doi.org/10.3847/1538-4357/ab5c1c)
- Wang, J.-W., Lai, S.-P., Eswaraiah, C., et al. 2019, ApJ, 876, 42, doi: [10.3847/1538-4357/ab13a2](https://doi.org/10.3847/1538-4357/ab13a2)
- Ward-Thompson, D., Pattle, K., Bastien, P., et al. 2017, ApJ, 842, 66, doi: [10.3847/1538-4357/aa70a0](https://doi.org/10.3847/1538-4357/aa70a0)
- Wardle, J. F. C., & Kronberg, P. P. 1974, ApJ, 194, 249, doi: [10.1086/153240](https://doi.org/10.1086/153240)
- Watt, S., & Mundy, L. G. 1999, ApJS, 125, 143, doi: [10.1086/313273](https://doi.org/10.1086/313273)
- Williams, G. M., Peretto, N., Avison, A., Duarte-Cabral, A., & Fuller, G. A. 2018, A&A, 613, A11, doi: [10.1051/0004-6361/201731587](https://doi.org/10.1051/0004-6361/201731587)
- Yuan, L., Li, G.-X., Zhu, M., et al. 2020, A&A, 637, A67, doi: [10.1051/0004-6361/201936625](https://doi.org/10.1051/0004-6361/201936625)